Computer Methods in Applied Mechanics and Engineering 426 (2024) 116988

Contents lists available at ScienceDirect

Comput. Methods Appl. Mech. Engrg.

journal homepage: www.elsevier.com/locate/cma

Nonlinear elasticity with the Shifted Boundary Method

Nabil M. Atallah [a,b], Guglielmo Scovazzi [a,*]

[a] Department of Civil and Environmental Engineering, Duke University, Durham, North Carolina 27708, USA
[b] Lawrence Livermore National Laboratory, Livermore (CA), USA

ARTICLE INFO

Keywords:
Unfitted finite elements
Shifted boundary method
Imaging-to-computing
Approximate boundary conditions
Complex geometry
Nonlinear solid mechanics

ABSTRACT

We propose a new unfitted/immersed computational framework for nonlinear solid mechanics, which bypasses the complexities associated with the generation of CAD representations and subsequent body-fitted meshing. This approach allows to speed up the cycle of design and analysis in complex geometry and requires relatively simple computer graphics representations of the surface geometries to be simulated, such as the Standard Tessellation Language (STL format). Complex data structures and integration on cut elements are avoided by means of an approximate boundary representation and a modification (shifting) of the boundary conditions to maintain optimal accuracy. An extensive set of computational experiments in two and three dimensions is included.

1. Introduction and overview

When considering the broader field of computational solid mechanics, one of the long-standing challenges is the simulation of shapes of complex geometry. Historically, Finite Element Analysis (FEA) provided accurate answers to geometrically complex problems in mechanics, and relied on unstructured mesh generation techniques to fit the computational grids to the shapes to be simulated. In fact, one of the strengths of FEA is the ability to impose boundary conditions on relatively complex geometries in a seamless and accurate way.

However, in recent years, topology optimization and related methods produced three-dimensional designs of geometric complexity that vastly surpassed prior examples, testing to the limit modern mesh generation techniques. On a parallel line of developments, computations started to routinely be performed on geometries acquired using a number of emerging biomedical and seismic imaging techniques. In this case, image segmentation and conversion to traditional geometric formats in Computer Aided Design (CAD) resulted in labor-intensive and time-consuming workflows. More recently, the development of digital twins of manufactured mechanical systems has also relied on imaging techniques to scan the actual geometry of the components under operating conditions, with the purpose of feeding this information to FEA models for performance/reliability prediction.

In the last decade, a variety of new embedded/immersed geometry approaches [1–3] have been proposed to further speed up design and analysis in complex geometry. These approaches started from the realization that the generation of CAD geometrical representations can still be a costly phase in the overall design and analysis process, especially if the geometry is obtained from the pixels/voxels that are the result of two/three-dimensional image reconstruction techniques. These approaches rapidly spread their area of application to problems in which CAD representations are more easily available, and showed great promise when combined with topology optimization [4–6]. These methods are based on: (1) the use of exact cut-cell geometry representations to construct the solution space and (2) the Nitsche's method [7] for consistent weak boundary enforcement [8].

* Corresponding author.
E-mail addresses: atallah1@llnl.gov (N.M. Atallah), guglielmo.scovazzi@duke.edu (G. Scovazzi).

https://doi.org/10.1016/j.cma.2024.116988
Received 5 November 2023; Received in revised form 14 March 2024; Accepted 5 April 2024
Available online 11 April 2024

Although these methods have been designed for a completely different purpose, they have borrowed some ideas from extended/enriched/unfitted methods for fracture mechanics [9]: we do not even attempt an account of the developments of the latter, which are peripheral to the discussion here. We refer an interested reader to [10–14] where a broader introduction is presented, although references to the massive amount of existing work on embedded discretizations for fracture mechanics may still lack completeness.

About two decades ago, Iso-Geometric Analysis (IGA) [15,16] was proposed as an alternative paradigm, in which NURBS or T-Spline functions are used to build discrete approximation spaces directly on the CAD representation, somewhat avoiding the costly operation of generating body-fitted grids. However, when the level of complexity of geometric shapes is large, Immerso-Geometric Methods [17–24] (i.e., immersed methods based on IGA approximation spaces) seem the preferred choice in the IGA community.

In this work, we propose a new immersed geometry approach to nonlinear solid mechanics, based on the Shifted Boundary Method (SBM) [10–12,14,25], in which the complex geometry to be simulated is immersed in a pre-existing grid, and boundary conditions are enforced on a surrogate boundary (the red segmented curve, in Fig. 1(a)), which lies in proximity of the true boundary (the blue curve, in Fig. 1(a)). This strategy has the advantage of bypassing the labor-intensive phase of CAD/mesh generation, since a simple representation of the surface geometry is sufficient to setup computations. For example, the proposed method works well with the Standard Tessellation Language (or STL format, common in computer graphics), which is based on collections of disconnected triangles in three dimensions.

One surprising aspect of the proposed approach is that the geometric representations of boundaries may not even need to be watertight on a fine scale, as long as their resolution is finer than the resolution of the grids utilized in simulations. More details on this aspect will be presented in the section of this article on numerical experiments.

The SBM approach bypasses two common issues stemming from the presence of cut cells in the computational domain, which have somewhat limited the broader application of immersed techniques in the engineering practice:

a. For body-fitted approaches, employing Nitsche's method does not adversely affect the conditioning of the system matrix. However, in the case of embedded finite elements, due to the arbitrariness of the size of the cut elements, naïve approaches suffer from numerical instabilities and poor matrix conditioning problems. A number of approaches have addressed this issue in recent years [26–29], but the geometric construction of the partial elements cut by the embedded boundary typically remains a complex and computationally intensive process.
b. The construction of more complex data structures and appropriately constructed quadrature formulas to integrate the variational equations on cut cell is challenging, and typically relies on the use of sub-triangulations (an approach that somewhat defeats the purpose of immersed methods) or the development of complex quadrature formulas directly in physical space (since it is not possible to define the parent domain of a cut element of arbitrary shape).

In the Shifted Boundary Method, boundary conditions of optimal accuracy are imposed on the surrogate boundary by means of Taylor extrapolations that account for the discrepancy of location between the surrogate and true boundary. Numerical results for the Poisson and Stokes problems [10] showed optimal convergence rates and adequate conditioning of the algebraic systems of equations. Afterwards, the SBM was extended to the advection/diffusion equation and the laminar and turbulent incompressible Navier–Stokes equations with static [11] and moving interfaces [13]. In addition to hyperbolic systems such as wave propagation problems in acoustics and shallow water flows [12]. The authors of [25] proposed a number of strategies to increase the accuracy of the method in elliptic problems and the authors of [14] presented a complete numerical analysis of the SBM for the Stokes problem (the analysis of the Poisson problem was already presented in [10]). A high-order version of the SBM was proposed [30] and a penalty-free version of the SBM was developed in [31].

The SBM was applied to linear elasticity problems [32] and interface/fracture mechanics problems [33–36], for which it was proved stable and convergent. More recently, the SBM was applied in combination with a material point method [37] and a level-set reinitialization technique [38].

When considering solid mechanics problems, the enforcement of Neumann conditions becomes crucial, since traction (or traction-free) boundary conditions are quite common on the majority of the boundary surfaces defining the geometry. Unfortunately, if a displacement-based, irreducible formulation of the SBM is used in combination with piecewise linear finite element spaces, it is not possible to accurately enforce traction boundary conditions, as they require a Taylor extrapolation of the derivative of the stress, that is, the Hessian of the displacement field. In this work, we propose to circumvent this issue by resorting to a mixed formulation, defined only on the layer of elements neighboring the surrogate (approximate) boundary and with the displacement and the first Piola stress tensor as unknowns. The mixed formulation on this layer of elements is then weakly (i.e., variationally) coupled to the rest of the computational domain, where a standard primal (displacement) formulation is applied. The net result is an improved formulation that maintains the computational cost of the base primal formulation, but allows for an accurate imposition of immersed traction boundary conditions.

An additional complexity associated specifically to nonlinear mechanics problems, is that the computational grid deforms with the motion of the material. This implies that both the surrogate and true boundaries deform as the loads are applied to the structure. To consistently construct the extrapolation operators required to apply the (shifted) boundary conditions, we pose the variational formulation in the original configuration of the solid body, and perform the Taylor expansions there. In principle, it is possible to map the proposed variational formulation to the current configuration of the solid body, using an updated-Lagrangian approach, which is not pursued in the present work.

More broadly, the general tradeoff of the SBM is that integration and data management of cut cells is completely avoided, at the expense of variational formulations that include additional terms with respect to the corresponding cutFEMs, Immerso-Geometric

and Finite Cell Methods. The SBM offers an additional important advantage over these methods, since in nonlinear mechanics the evaluation of complex constitutive models at quadrature points may represent a large portion of the computation. CutFEMs, Immerso-Geometric and Finite Cell Methods typically require a much larger number of quadrature points on cut cells, with respect to the standard quadrature rules utilized on full cells. Instead, the SBM does not require to change the integration rules with respect to a body fitted finite element method, because there are no cut cells. To modify an existing body-fitted finite element method into a SBM, all that is needed are the two steps detailed below:

1. A preprocessing phase in which the surrogate boundary is defined, as well as its (vector) distance from the true boundary (a step that can be achieved using either modified closed-point projection techniques, level-set approaches, or variational methods [39]).
2. The modification of the boundary conditions of the original body-fitted variational formulation using Taylor expansions of the solution along the distance vector.

These two steps are usually much less complex to implement than the data structures for the geometrical description of volumes/boundaries of cut cells and the corresponding numerical integration strategies.

This article is organized as follows: Section 2 introduces the governing equations of static nonlinear elasticity; Section 3 presents the formalism of the Shifted Boundary Method, a preliminary mixed displacement-Piola stress variational formulation and the more efficient shifted boundary formulation in which the mixed form is restricted to a single layer of elements near the surrogate boundary (Section 3.4); Section 4 presents a comprehensive set of numerical tests of accuracy and robustness in two and three dimensions; and, finally conclusions are summarized in Section 5.

2. Equations of nonlinear elasticity

We consider problems in nonlinear (finite strain) hyperelasticity, in the Lagrangian reference frame. In what follows, we will consider a mixed formulation in which the displacement and Piola stress are solved as nodal unknowns. This formulation is defined only on the layer of elements neighboring the surrogate (approximate) boundary, as a way to reconstruct second-order derivatives of the displacements in a stable, accurate and robust way. The mixed formulation on this layer of elements is then weakly (i.e., variationally) coupled to the rest of the computational domain, where a standard primal (displacement) formulation is applied.

2.1. Governing equations in the original configuration

Let us indicate the initial and current configurations of the body by Ω_0 and Ω, respectively. Ω and Ω_0 are connected open sets in $\mathbb{R}^{n_d}$ with Lipschitz boundaries ($n_d = 2, 3$ indicates the number of spatial dimensions). The deformation of the body is characterized by the *motion*

$$\begin{aligned} \boldsymbol{\varphi} &: \Omega_0 \to \Omega = \boldsymbol{\varphi}(\Omega_0) \\ &\boldsymbol{X} \longmapsto \boldsymbol{x} = \boldsymbol{\varphi}(\boldsymbol{X}) \,, \forall \boldsymbol{X} \in \Omega_0 \,, \end{aligned}$$

which maps the material coordinate $\boldsymbol{X}$, representing the initial position of an infinitesimal material particle of the body, to $\boldsymbol{x}$, the position of the same particle in the current configuration. We denote the boundaries of these domains by $\Gamma_0 = \partial\Omega_0$ and $\Gamma = \partial\Omega$ and always assume that $\boldsymbol{\varphi}(\Gamma_0) = \Gamma$. We assume that $\boldsymbol{\varphi}$ is smooth and invertible, such that the *deformation gradient* $\boldsymbol{F} = \nabla_{\boldsymbol{X}} \boldsymbol{\varphi}$, the deformation *Jacobian determinant* $J = \det \boldsymbol{F} > 0$ and the *right Cauchy–Green strain tensor* $\boldsymbol{C} = \boldsymbol{F}^T \boldsymbol{F}$ are always well defined. Note that $\nabla_{\boldsymbol{X}}$ indicates the gradient with respect to the original configuration coordinate $\boldsymbol{X}$.

We denote by ρ the density and by $\boldsymbol{u} = \boldsymbol{x} - \boldsymbol{X}$ the displacement. We recall the relation $\boldsymbol{P} = J\,\boldsymbol{\sigma}\,\boldsymbol{F}^{-T} = \boldsymbol{\sigma}\,\mathbf{cof}\,\boldsymbol{F}$, between $\boldsymbol{\sigma}$, the *Cauchy stress tensor* and $\boldsymbol{P}$, the *first Piola–Kirchhoff stress tensor*, as well as the definition $\boldsymbol{S} = \boldsymbol{F}^{-1}\boldsymbol{P}$, of the *second Piola–Kirchhoff (symmetric) stress tensor* $\boldsymbol{S}$. In what follows, we will omit the dependency $\boldsymbol{F} = \boldsymbol{F}(\boldsymbol{u})$, which will always be implied.

The static equilibrium condition over the original body configuration Ω_0 can be written as

$$-\nabla_{\boldsymbol{X}} \cdot \boldsymbol{P} = \rho_0 \boldsymbol{b} \,, \tag{1a}$$

where $\nabla_{\boldsymbol{X}} \cdot$ is the divergence operator in the original configuration. We complement equation (1a) with the identity

$$\boldsymbol{P} - \boldsymbol{P}(\boldsymbol{u}) = \boldsymbol{0} \,, \tag{1b}$$

where $\boldsymbol{P}(\boldsymbol{u})$ indicates the first Piola–Kirchhoff stress expressed as a function of $\boldsymbol{u}$.

The set of governing equations (1) is a mixed system, in terms of the unknown displacement vector $\boldsymbol{u}$ and first Piola–Kirchhoff stress tensor $\boldsymbol{P}$, and must be complemented by a specific constitutive relationship $\boldsymbol{P}(\boldsymbol{u})$ and appropriate boundary conditions.

2.2. Boundary conditions

For the problem under consideration, the boundary conditions are specified assuming that the boundary $\Gamma_0 = \partial\Omega_0$ is partitioned as $\overline{\Gamma_{0,D} \cup \Gamma_{0,N}}$ with $\Gamma_{0,D} \cap \Gamma_{0,N} = \emptyset$. An analogous partition exists for the boundary observed in the current configuration, namely, $\overline{\Gamma_D \cup \Gamma_N}$ with $\Gamma_D \cap \Gamma_N = \emptyset$. In the original configuration, the displacement boundary conditions can be expressed as

$$\boldsymbol{u} = \boldsymbol{u}_D(\boldsymbol{X}) \,, \qquad \text{on } \Gamma_{0,D} \,, \tag{2}$$

and the traction boundary conditions can be expressed as

$$\boldsymbol{P}\,\boldsymbol{N} = \boldsymbol{T}_N(\boldsymbol{X}) \,, \qquad \text{on } \Gamma_{0,N} \,, \tag{3}$$

where $\boldsymbol{T}_N$ is the normal traction and $\boldsymbol{N}$ is the outward-pointing normal to the boundary Γ_0. We also recall Nanson's formula $\boldsymbol{n}\,\mathrm{d}\Gamma = \mathbf{cof}\boldsymbol{F}\,\boldsymbol{N}\,\mathrm{d}\Gamma_0$, where $\boldsymbol{n}$ is the boundary outward-pointing normal to the current configuration boundary Γ.

2.3. Hyperelastic constitutive models

We consider isotropic hyperelastic compressible constitutive models, often used to characterize metal alloys. Under the assumption that any volumetric state of stress will change the volume of a material but not its shape, the *Helmholtz free energy density* Ψ, or *strain energy density* function, can be decomposed into a volumetric component U and a deviatoric component W:

$$\Psi = W(\bar{I}_1, \bar{I}_2) + U(J) \,, \tag{4}$$

where $\bar{I}_1 = J^{-2/3} I_1$, $\bar{I}_2 = J^{-4/3} I_2$, $I_1 = \mathrm{tr}(\boldsymbol{C})$ is the *First Principal Invariant* of $\boldsymbol{C}$, and $I_2 = (1/2)\left(\mathrm{tr}(\boldsymbol{C})^2 - \mathrm{tr}(\boldsymbol{C}^2)\right)$ is the *Second Principal Invariant* $\boldsymbol{C}$. In this work, W and U are adopted from [40,41] and given as

$$W(\bar{I}_1, \bar{I}_2) := \frac{\mu}{2}\left(\bar{I}_1 - n_d\right) \,, \tag{5}$$

$$U(J) := \kappa\,(J\ln(J) - J + 1) \,, \tag{6}$$

where μ and κ are the nominal shear and bulk moduli respectively. With classical arguments, the first Piola–Kirchhoff stress tensor can be shown to relate to the derivative of the strain energy function according to

$$\boldsymbol{P} = \frac{\partial \Psi}{\partial \boldsymbol{F}} = \frac{\partial W}{\partial \boldsymbol{F}} + \frac{\partial U}{\partial \boldsymbol{F}} = \boldsymbol{P}_{\mathrm{dev}} + \boldsymbol{P}_{\mathrm{vol}}. \tag{7}$$

where $\boldsymbol{P}_{\mathrm{dev}} = \frac{\partial W}{\partial \boldsymbol{F}}$ and $\boldsymbol{P}_{\mathrm{vol}} = \frac{\partial U}{\partial \boldsymbol{F}}$.

3. The shifted boundary method

3.1. Preliminaries: The true domain, the surrogate domain and maps

Consider a closed domain $\mathscr{D}_0$ such that $\mathrm{clos}(\Omega_0) \subseteq \mathscr{D}_0$ and we introduce a family of admissible and shape-regular triangulations of $\mathscr{D}_0$. Then, we restrict each triangulation $\mathscr{T}^h$ by selecting those elements that are contained in $\mathrm{clos}(\Omega_0)$, i.e., we form

$$\tilde{\mathscr{T}}^h := \{T \in \mathscr{T}^h \,:\, T \subset \mathrm{clos}(\Omega_0)\}.$$

This identifies the *surrogate domain*

$$\tilde{\Omega}_0^h := \mathrm{int}\Big(\bigcup_{T \in \tilde{\mathscr{T}}^h} T\Big) \subseteq \Omega_0 \,, \tag{8}$$

with *surrogate boundary* $\tilde{\Gamma}_0^h := \partial\tilde{\Omega}_0^h$ and outward-oriented unit normal vector $\tilde{\boldsymbol{N}}$ to $\tilde{\Gamma}_0^h$. Obviously, $\tilde{\mathscr{T}}^h$ is an admissible and shape-regular triangulation of $\tilde{\Omega}_0^h$ (see Fig. 1(a)). We indicate by h_T (h_T^i, resp.) the circumscribed diameter (inscribed diameter, resp.) of an element $T \in \tilde{\mathscr{T}}^h$ and by h (h^i, resp.) the piecewise constant function in $\tilde{\Omega}_0^h$ such that $h_{|T} = h_T$ ($h^i_{|T} = h^i_T$, resp.) for all $T \in \tilde{\mathscr{T}}^h$. We also introduce the mesh size parameter

$$h_\perp := \frac{\mathrm{meas}_{n_d}(T)}{\mathrm{meas}_{n_d-1}(\tilde{\gamma}_e)} \,, \tag{9}$$

for every edge $\tilde{\gamma}_e \in \tilde{\Gamma}_0^h$ with $\partial T \cap \tilde{\gamma}_e \neq \emptyset$, $T \in \tilde{\mathscr{T}}^h$. $h_\perp$ will be used to construct variational terms on the surrogate boundary.

We now define a mapping

$$\boldsymbol{M}^h : \tilde{\Gamma}_0^h \to \Gamma_0 \,, \tag{10a}$$

$$\tilde{\boldsymbol{X}} \mapsto \boldsymbol{X} \,, \tag{10b}$$

which associates to any point $\tilde{\boldsymbol{X}} \in \tilde{\Gamma}_0^h$ on the surrogate boundary a point $\boldsymbol{X} = \boldsymbol{M}^h(\tilde{\boldsymbol{X}})$ on the physical boundary Γ_0. Through $\boldsymbol{M}^h$, a distance vector function $\boldsymbol{D}_{\boldsymbol{M}^h}$ can be defined as

$$\boldsymbol{D}_{\boldsymbol{M}^h}(\tilde{\boldsymbol{X}}) = \boldsymbol{X} - \tilde{\boldsymbol{X}} = [\,\boldsymbol{M}^h - \boldsymbol{I}\,](\tilde{\boldsymbol{X}}). \tag{11}$$

For the sake of simplicity, we set $\boldsymbol{D} = \boldsymbol{D}_{\boldsymbol{M}^h}$ where $\boldsymbol{D} = \|\boldsymbol{D}\|\boldsymbol{\nu}$ and $\boldsymbol{\nu}$ is a unit vector.

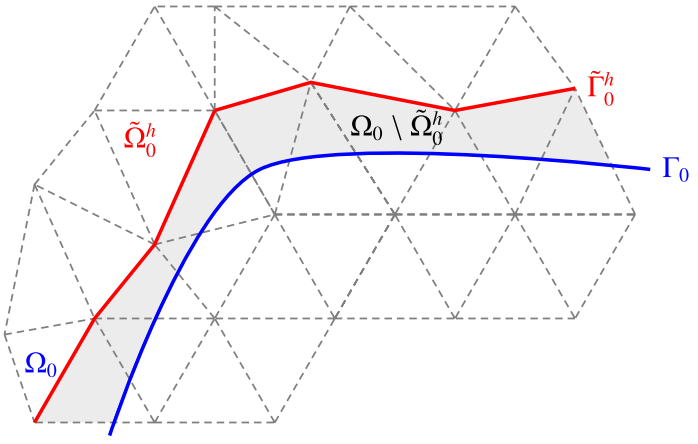

(a) The true domain Ω_0, the surrogate domain $\tilde{\Omega}_0^h \subset \Omega_0$, the true boundary Γ_0, and the surrogate boundary $\tilde{\Gamma}_0^h$.

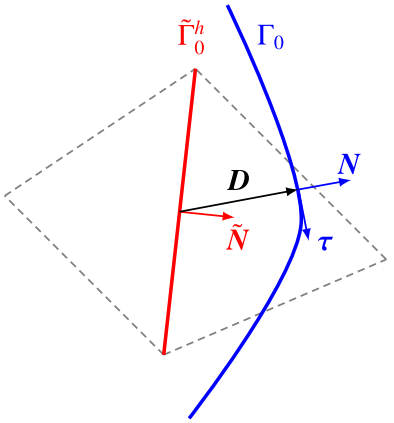

(b) The distance vector $\boldsymbol{D}$, the true normal $\boldsymbol{N}$, the true tangent $\boldsymbol{\tau}$, and the surrogate normal $\tilde{\boldsymbol{N}}$.

Fig. 1. The surrogate domain, its boundary, and the distance vector $\boldsymbol{D}$. (For interpretation of the references to color in this figure legend, the reader is referred to the web version of this article.)

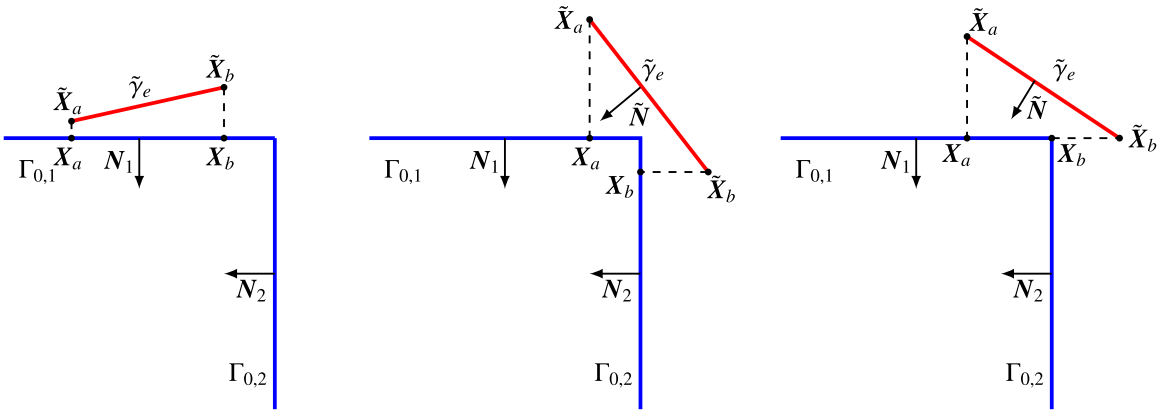

(a) Case 1. (b) Case 2. (c) Case 3.

Fig. 2. Cases involved in the strategy for assigning a sideset to the surrogate edge $\tilde{\gamma}_e$.

Remark 1. There are other strategies in the definition of the map $\boldsymbol{M}^h$ and, correspondingly, the distance vector $\boldsymbol{D}$. Among them is a level set description of the true boundary, in which $\boldsymbol{D}$ is defined by means of a distance function.

Since Γ_0 is partitioned into a Dirichlet boundary $\Gamma_{0,D}$ and a Neumann boundary $\Gamma_{0,N}$ it becomes important to define a strategy to identify a surrogate edge $\tilde{\gamma}_e \subset \tilde{\Gamma}_0^h$ as belonging to $\Gamma_{0,D}$ or $\Gamma_{0,N}$. To this end, we partition $\tilde{\Gamma}_0^h$ as $\overline{\tilde{\Gamma}_{0,D}^h \cup \tilde{\Gamma}_{0,N}^h}$ with $\tilde{\Gamma}_{0,D}^h \cap \tilde{\Gamma}_{0,N}^h = \emptyset$, where

$$\tilde{\Gamma}_{0,D}^h = \{\tilde{\gamma}_e \subseteq \tilde{\Gamma}_0^h \,:\, \boldsymbol{M}^h(\tilde{\gamma}_e) \subseteq \Gamma_{0;D}\} \tag{12}$$

and $\tilde{\Gamma}_{0,N}^h = \tilde{\Gamma}_0^h \setminus \tilde{\Gamma}_{0,D}^h$.

3.1.1. Boundaries with edges, corners, or multiple boundary conditions

We describe now in more detail the treatment of boundaries with edges or corners, as they are of importance in practical engineering applications. Let us assume that the boundary Γ_0 of the original domain Ω_0 is partitioned into K subsets $\Gamma_{0,k}$, $k = 1, \dots, K$, hereafter termed *sidesets*, with the following properties:

1. Each $\Gamma_{0,k}$ is relatively closed in Γ, and satisfies $\cup_{k=1}^K \Gamma_{0,k} = \Gamma$, $\operatorname{int}\Gamma_{0,k} \cap \operatorname{int}\Gamma_{0,l} = \emptyset$ for $k \neq l$.
2. Each $\Gamma_{0,k}$ is "smooth", in the sense that the normal unit vector $\boldsymbol{N}_k$ (pointing outward) exists at each $\boldsymbol{X} \in \Gamma_{0,k}$ and varies in a continuous manner.
3. The assigned boundary condition data is a smooth function on each $\Gamma_{0,k}$.

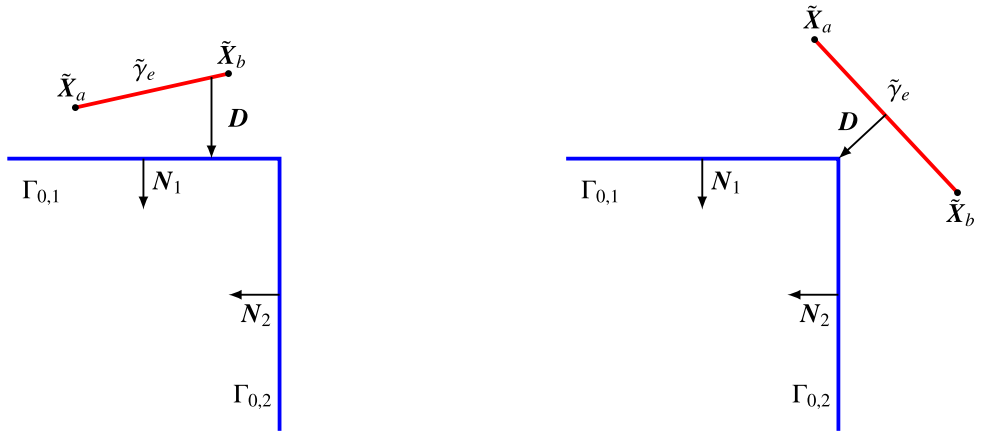

(a) Distance vector $\boldsymbol{D}$ aligned with $\boldsymbol{N}_1$.

(b) Distance vector $\boldsymbol{D}$ not aligned with either $\boldsymbol{N}_1$ or $\boldsymbol{N}_2$.

Fig. 3. The distance vector $\boldsymbol{D}$ and the normal vector $\boldsymbol{N}$ to Γ_0.

We aim at associating a unique sideset to each edge (in two dimensions) or face (in three dimensions) of the triangulation $\tilde{\mathcal{T}}^h$ that is sitting on the surrogate boundary $\tilde{\Gamma}_0^h$. All the information needed to define the transported boundary data on the edge/face will be drawn from the associated sideset.

Consider the case of an edge $\tilde{\gamma}_e \subset \tilde{\Gamma}_0^h$ in two dimensions (the three-dimensional case can be handled similarly) with $\tilde{\boldsymbol{N}}$ as its unit normal vector. Let $\tilde{\boldsymbol{X}}_a$, $\tilde{\boldsymbol{X}}_b$ be the endpoints of $\tilde{\gamma}_e$ and $\boldsymbol{X}_a$, $\boldsymbol{X}_b$ be their respective closest-point projections upon Γ_0. Finally, let L be the set of sidesets that $\boldsymbol{X}_a$ and $\boldsymbol{X}_b$ belong to. To associate a unique sideset $\Gamma_{m(\tilde{\gamma}_e)}$ to $\tilde{\gamma}_e$, the following cases arise:

(i) If $\boldsymbol{X}_a$ and $\boldsymbol{X}_b$ belong to the same unique sideset, say $\Gamma_{0,1}$, then the set L will have a single, element, namely $\Gamma_{0,1}$, and thus $\tilde{\gamma}_e$ is associated with it (Fig. 2(a)).

(ii) If $\boldsymbol{X}_a$ and $\boldsymbol{X}_b$ belong to different, unique sidesets, say $\Gamma_{0,1}$ and $\Gamma_{0,2}$, then the set L will consist of $\Gamma_{0,1}$ and $\Gamma_{0,2}$ (Fig. 2(b)). In such a case, we associate $\tilde{\gamma}_e$ with the sideset $\Gamma_{0,k}$ in L such that

$$\Gamma_{0,k} = \arg \max_{\Gamma_{0,s} \in L} f(\Gamma_{0,s}) \tag{13}$$

where $f(\Gamma_{0,s}) = \sum_{i=a,b} \tilde{\boldsymbol{N}} \cdot \boldsymbol{N}_{\Gamma_{0,s}}(\boldsymbol{X}_i)$.

(iii) If $\boldsymbol{X}_a$ (or $\boldsymbol{X}_b$) belongs to the intersection of two sidesets, say $\Gamma_{0,1}$ and $\Gamma_{0,2}$, then both such sidesets are added to set L. At this point, we refer to case (ii) for associating $\tilde{\gamma}_e$ with a sideset (Fig. 2(c)).

At last, we define the mapping $\boldsymbol{M}^h$ on $\tilde{\gamma}_e$ by setting, for any $\tilde{\boldsymbol{X}} \in \tilde{\gamma}_e$,

$$\boldsymbol{M}^h(\tilde{\boldsymbol{X}}) := \text{the closest-point projection of } \tilde{\boldsymbol{X}} \text{ upon } \Gamma_{m(\tilde{\gamma}_e)}\,. \tag{14}$$

Remark 2. We make two observations. (i) According to the given definition, $\boldsymbol{M}^h$ may be multi-valued at the intersection of two edges. However, this has no effect at all since $\boldsymbol{M}^h$ appears in the boundary integrals which are computed edge-wise. (ii) If $\boldsymbol{M}^h(\tilde{\boldsymbol{X}})$ falls in the interior of a sideset $\Gamma_{0,k}$ and coincides with the closest-point projection of $\tilde{\boldsymbol{X}}$ *upon the whole* Γ, then the vector $\boldsymbol{D}$ is aligned with $\boldsymbol{N}_k$ (Fig. 3(a)). Otherwise, it may not be aligned (Fig. 3(b)).

3.2. General strategy

In the SBM approach, the governing equations (1) are discretized on $\tilde{\Omega}_0^h$ rather than Ω_0, with the challenge of appropriately imposing on $\tilde{\Gamma}_0^h$ boundary conditions that would mimic (2) and (3). To this end, we resort to the idea introduced in [10] and perform a first-order Taylor expansion of $\boldsymbol{u}$ and $\boldsymbol{P}$ at their respective surrogate boundaries in order to "shift" the boundary conditions from Γ to $\tilde{\Gamma}_0^h$. Introducing the extension operators

$$\mathbb{E}\boldsymbol{u}_D(\tilde{\boldsymbol{X}}) := \boldsymbol{u}_D(\boldsymbol{M}^h(\tilde{\boldsymbol{X}}))\,, \tag{15}$$

on $\tilde{\Gamma}_{0,D}^h$, and

$$\mathbb{E}\boldsymbol{T}_N(\tilde{\boldsymbol{X}}) := \boldsymbol{T}_N(\boldsymbol{M}^h(\tilde{\boldsymbol{X}}))\,, \tag{16}$$

$$\mathbb{E}\boldsymbol{N}(\tilde{\boldsymbol{X}}) := \boldsymbol{N}(\boldsymbol{M}^h(\tilde{\boldsymbol{X}}))\,, \tag{17}$$

on $\tilde{\Gamma}^h_{0,N}$, we can define a *shifted* approximation of the boundary conditions as follows:

$$\mathcal{S}^h_D \boldsymbol{u} = \mathbb{E}\boldsymbol{u}_D \,, \qquad \text{on } \tilde{\Gamma}^h_{0,D} \,, \tag{18a}$$

$$\left(\mathcal{S}^h_N \boldsymbol{P}\right) \mathbb{E}\boldsymbol{N} = \mathbb{E}\boldsymbol{T}_N \,, \qquad \text{on } \tilde{\Gamma}^h_{0,N}. \tag{18b}$$

where the boundary shift operators have been defined by means of Taylor expansions up to quadratic order of accuracy. Namely:

$$\mathcal{S}^h_D \boldsymbol{u} := \boldsymbol{u} + (\nabla_{\boldsymbol{X}} \boldsymbol{u})\boldsymbol{D} \,, \qquad \text{on } \tilde{\Gamma}^h_{0,D} \,, \tag{19a}$$

$$\mathcal{S}^h_N \boldsymbol{P} := \boldsymbol{P} + (\nabla_{\boldsymbol{X}} \boldsymbol{P})\boldsymbol{D} \,, \qquad \text{on } \tilde{\Gamma}^h_{0,N} \,. \tag{19b}$$

If accuracy higher than quadratic is required, then the polynomial order of the finite element space must be increased and, correspondingly, additional terms in the Taylor expansions need to be added. In what follows, whenever it does not cause confusion, the symbol $\mathbb{E}$ will be omitted from the extended quantities, and we would write $\boldsymbol{N}$, $\boldsymbol{u}_D$ and $\boldsymbol{T}_N$ in place of $\mathbb{E}\boldsymbol{N}$, $\mathbb{E}\boldsymbol{u}_D$ and $\mathbb{E}\boldsymbol{T}_N$, respectively.

3.3. A preliminary mixed shifted formulation for nonlinear elasticity

In this section, we introduce a mixed variational formulation for nonlinear elasticity. With some notable exceptions (see e.g., [42–56] and references therein) mixed formulations are less common than irreducible (primal) formulations, which rely only on the displacement unknown.

The motivation for a mixed formulation in the context of the Shifted Boundary Method is the ease of implementation of the Neumann boundary conditions (18b). The price to be paid with mixed formulations is an increase in the overall computational cost, although, at the same time, the stresses and strains are typically captured with higher accuracy and incompressibility constraints can be treated more robustly.

When higher-order or IGA discretizations are available, an alternative approach, discussed in [31], is to accept the loss of one order of accuracy with respect to optimal convergence and avoid the mixed formulation. While a reduction from second-order to first-order accuracy might be deemed unacceptable for a low-order finite element discretization, the same might not be said for higher-order formulations, which rely on high-order body-fitted grids to maintain accuracy. In the latter case the loss of just one order of accuracy might be a good compromise if high-order body fitted meshes can be avoided.

Section 3.4 shows an additional alternative, in which the mixed formulation is applied it *only* over a small layer of elements near the boundary. Then the overall computational cost of the shifted imposition of Neumann conditions can be drastically reduced. This specific version of the shifted boundary approach becomes comparable in computational cost to an irreducible (primal) formulation.

Observe also that the simple nodal projection of the element stress (L^2-projection) and subsequent application of the Taylor expansion is not an option. In fact, nodal projection is equivalent to an unstable mixed formulation and leads to suboptimal convergence rates for the displacements, in a number of preliminary tests not reported here for the sake of brevity.

Thus, our first step is to describe a general mixed form of the Shifted Boundary Method that applies to the entire surrogate domain $\tilde{\Omega}^h_0$. Note that other choices of mixed formulations are applicable for the same purpose [42–47,50,51,53–56], and the discussion to follow in Section 3.4 is not confined to the specific mixed formulation considered here.

Let $\mathbb{V}^h_{\boldsymbol{u}}(\tilde{\Omega}^h_0)$ and $\mathbb{V}^h_{\boldsymbol{P}}(\tilde{\Omega}^h_0)$ be the discrete, piecewise-linear, globally continuous trial and test function spaces for the displacement $\boldsymbol{u}^h$ and the first Piola–Kirchhoff stress tensor $\boldsymbol{P}^h$. Namely,

$$\mathbb{V}^h_{\boldsymbol{u}}(\tilde{\Omega}^h_0) = \{\boldsymbol{v}^h \in (C^0(\tilde{\Omega}^h_0))^{n_d} \,:\, \boldsymbol{v}^h_{|T} \in (\mathscr{P}^1(T))^{n_d} \,,\ \forall T \in \tilde{\mathscr{T}}^h\} \,, \tag{20a}$$

$$\mathbb{V}^h_{\boldsymbol{P}}(\tilde{\Omega}^h_0) = \{\boldsymbol{Q}^h \in (C^0(\tilde{\Omega}^h_0))^{n_d \times n_d} \,:\, \boldsymbol{Q}^h_{|T} \in (\mathscr{P}^1(T))^{n_d \times n_d} \,,\ \forall T \in \tilde{\mathscr{T}}^h\} \,, \tag{20b}$$

where $\mathscr{P}^1(T)$ is the space of linear polynomial functions over the element T.

Multiplying the governing equations (1a)–(1b) by the test function pair $[\boldsymbol{\phi}^h, \boldsymbol{\psi}^h] \in \mathbb{V}^h_{\boldsymbol{u}}(\tilde{\Omega}^h_0) \times \mathbb{V}^h_{\boldsymbol{P}}(\tilde{\Omega}^h_0)$ and integrating by parts, yields

$$0 = (\boldsymbol{P}^h, \nabla_{\boldsymbol{X}} \boldsymbol{\phi}^h)_{\tilde{\Omega}^h_0} - \langle \boldsymbol{P}^h \tilde{\boldsymbol{N}}, \boldsymbol{\phi}^h \rangle_{\tilde{\Gamma}^h_{0,D}} - \langle \boldsymbol{P}^h \tilde{\boldsymbol{N}}, \boldsymbol{\phi}^h \rangle_{\tilde{\Gamma}^h_{0,N}} - (\rho_0 \boldsymbol{b}, \boldsymbol{\phi}^h)_{\tilde{\Omega}^h_0} + (\boldsymbol{P}^h - \boldsymbol{P}(\boldsymbol{u}^h), \boldsymbol{\psi}^h)_{\tilde{\Omega}^h_0} \,. \tag{21}$$

Decomposing the surrogate unit normal $\tilde{\boldsymbol{N}}$ as $\tilde{\boldsymbol{N}} = (\tilde{\boldsymbol{N}} \cdot \boldsymbol{N})\boldsymbol{N} + (\tilde{\boldsymbol{N}} \cdot \boldsymbol{\tau}_j)\boldsymbol{\tau}_j$, where $\boldsymbol{\tau}_j$ is a unit vector tangent to the true boundary surface and repeated index notation is implied, leads to a weak form of imposition of the Neumann conditions (19b). Namely:

$$\begin{aligned}
\langle \boldsymbol{P}^h \tilde{\boldsymbol{N}}, \boldsymbol{\phi}^h \rangle_{\tilde{\Gamma}^h_{0,N}} &= \langle (\tilde{\boldsymbol{N}} \cdot \boldsymbol{N}) \boldsymbol{P}^h \boldsymbol{N} + (\tilde{\boldsymbol{N}} \cdot \boldsymbol{\tau}_j) \boldsymbol{P}^h \boldsymbol{\tau}_j, \boldsymbol{\phi}^h \rangle_{\tilde{\Gamma}^h_{0,N}} \\
&= \langle (\tilde{\boldsymbol{N}} \cdot \boldsymbol{N}) \left(\boldsymbol{T}_N - \left((\nabla_{\boldsymbol{X}} \boldsymbol{P}^h) \boldsymbol{D} \right) \boldsymbol{N} \right) + (\tilde{\boldsymbol{N}} \cdot \boldsymbol{\tau}_j) \boldsymbol{P}^h \boldsymbol{\tau}_j, \boldsymbol{\phi}^h \rangle_{\tilde{\Gamma}^h_{0,N}} \\
&= \langle (\tilde{\boldsymbol{N}} \cdot \boldsymbol{N}) \left(\boldsymbol{T}_N - (\mathcal{S}^h_N \boldsymbol{P}^h) \boldsymbol{N} \right) + \boldsymbol{P}^h \tilde{\boldsymbol{N}}, \boldsymbol{\phi}^h \rangle_{\tilde{\Gamma}^h_{0,N}} \,.
\end{aligned} \tag{22}$$

We also add a penalty term on the Neumann boundary,

$$\langle \tau_N (\mathcal{S}^h_N(\boldsymbol{P}^h) \boldsymbol{N} - \boldsymbol{T}_N), (\tilde{\boldsymbol{N}} \cdot \boldsymbol{N})^2 (\mathcal{S}^h_N \boldsymbol{\psi}^h) \boldsymbol{N} \rangle_{\tilde{\Gamma}^h_{0,N}} \,, \tag{23}$$

for the purpose of enhancing the overall stability of the formulation; where $\tau_N = c_N\,\bar{l}(\Omega_0)$, $\bar{l}(\Omega_0)$ is the largest dimension of the bounding box of Ω_0, and c_N is a nondimensional positive constant. Dirichlet conditions can also be imposed in a weak sense, resorting to the Nitsche-type term

$$\langle(\mathcal{C}(\boldsymbol{u}^h)\,\boldsymbol{\psi}^h)\tilde{\boldsymbol{N}}\,,\,\mathcal{S}_D^h\boldsymbol{u}^h-\boldsymbol{u}_D\rangle_{\tilde{\Gamma}^h_{0,D}}+\alpha\,\langle\|\mathcal{C}_{\text{vol}}(\boldsymbol{u}^h)\|\,h_\perp^{-1}(\tilde{\boldsymbol{N}}\otimes\tilde{\boldsymbol{N}})\,\mathcal{S}_D^h\boldsymbol{\phi}^h\,,\,\mathcal{S}_D^h\boldsymbol{u}^h-\boldsymbol{u}_D\rangle_{\tilde{\Gamma}^h_{0,D}} \tag{24}$$

$$+\alpha\,\langle\|\mathcal{C}_{\text{dev}}(\boldsymbol{u}^h)\|\,h_\perp^{-1}(\boldsymbol{I}-\tilde{\boldsymbol{N}}\otimes\tilde{\boldsymbol{N}})\,\mathcal{S}_D^h\boldsymbol{\phi}^h\,,\,\mathcal{S}_D^h\boldsymbol{u}^h-\boldsymbol{u}_D\rangle_{\tilde{\Gamma}^h_{0,D}} \tag{25}$$

where $\mathcal{C}(\boldsymbol{u})=\partial\boldsymbol{P}^h(\boldsymbol{F})/\partial\boldsymbol{F}$, $\mathcal{C}(\boldsymbol{u})_{\text{dev}}=\partial\boldsymbol{P}^h_{\text{dev}}(\boldsymbol{F})/\partial\boldsymbol{F}$ and $\mathcal{C}(\boldsymbol{u})_{\text{vol}}=\partial\boldsymbol{P}^h_{\text{vol}}(\boldsymbol{F})/\partial\boldsymbol{F}$ are the (tangent) fourth-order elasticity tensors associated with the free-energy density Ψ, W and U respectively, with Frobenius norms $\|\mathcal{C}(\boldsymbol{u})\|$, $\|\mathcal{C}_{\text{dev}}(\boldsymbol{u})\|$ and $\|\mathcal{C}_{\text{vol}}(\boldsymbol{u})\|$, respectively. Finally, α is a nondimensional positive constant. Combining (22), (23) and (24) with (21), we obtain

$$\begin{aligned}0=\;&(\boldsymbol{P}^h,\nabla_{\boldsymbol{X}}\boldsymbol{\phi}^h)_{\tilde{\Omega}_0^h}-\langle\boldsymbol{P}^h\,\tilde{\boldsymbol{N}},\boldsymbol{\phi}^h\rangle_{\tilde{\Gamma}^h_{0,D}}-\langle(\tilde{\boldsymbol{N}}\cdot\boldsymbol{N})\,(\boldsymbol{T}_N-(\mathcal{S}_N^h\boldsymbol{P}^h)\boldsymbol{N})+\boldsymbol{P}^h\tilde{\boldsymbol{N}},\boldsymbol{\phi}^h\rangle_{\tilde{\Gamma}^h_{0,N}}-(\rho_0\boldsymbol{b},\boldsymbol{\phi}^h)_{\tilde{\Omega}_0^h}\\&+(\boldsymbol{P}^h-\boldsymbol{P}(\boldsymbol{u}^h),\boldsymbol{\psi}^h)_{\tilde{\Omega}_0^h}+\langle(\mathcal{C}(\boldsymbol{u}^h)\,\boldsymbol{\psi}^h)\tilde{\boldsymbol{N}}\,,\,\mathcal{S}_D^h\boldsymbol{u}^h-\boldsymbol{u}_D\rangle_{\tilde{\Gamma}^h_{0,D}}+\alpha\,\langle\|\mathcal{C}_{\text{vol}}(\boldsymbol{u}^h)\|\,h_\perp^{-1}(\tilde{\boldsymbol{N}}\otimes\tilde{\boldsymbol{N}})\,\mathcal{S}_D^h\boldsymbol{\phi}^h\,,\,\mathcal{S}_D^h\boldsymbol{u}^h-\boldsymbol{u}_D\rangle_{\tilde{\Gamma}^h_{0,D}}\\&+\alpha\,\langle\|\mathcal{C}_{\text{dev}}(\boldsymbol{u}^h)\|\,h_\perp^{-1}(\boldsymbol{I}-\tilde{\boldsymbol{N}}\otimes\tilde{\boldsymbol{N}})\,\mathcal{S}_D^h\boldsymbol{\phi}^h\,,\,\mathcal{S}_D^h\boldsymbol{u}^h-\boldsymbol{u}_D\rangle_{\tilde{\Gamma}^h_{0,D}}+\langle\tau_N(\mathcal{S}_N^h(\boldsymbol{P}^h)\boldsymbol{N}-\boldsymbol{T}_N),(\tilde{\boldsymbol{N}}\cdot\boldsymbol{N})^2(\mathcal{S}_N^h\boldsymbol{\psi}^h)\boldsymbol{N}\rangle_{\tilde{\Gamma}^h_{0,N}}\,.\end{aligned} \tag{26}$$

Observe that the approximation spaces $\mathbb{V}^h_{\boldsymbol{u}}(\tilde{\Omega}_0^h)$ and $\mathbb{V}^h_{\boldsymbol{P}}(\tilde{\Omega}_0^h)$ do not satisfy the inf-sup condition [57] in the linear limit, and instability may arise also in nonlinear computations. To circumvent this situation, we adopt a variational multiscale (VMS) approach [42,47,58] and add to (26) the stabilization terms

$$-\tau_{\boldsymbol{P}}(\,\boldsymbol{P}^h-\boldsymbol{P}^h(\boldsymbol{u}^h)\,,\,\boldsymbol{\psi}^h+\nabla_{\boldsymbol{X}}\boldsymbol{\phi}^h\,)_{\tilde{\Omega}_0^h}+\tau_{\boldsymbol{u}}(\,\nabla_{\boldsymbol{X}}\cdot\boldsymbol{P}^h+\rho_0\boldsymbol{b}\,,\,\nabla_{\boldsymbol{X}}\cdot\boldsymbol{\psi}\,)_{\tilde{\Omega}_0^h}. \tag{27}$$

In the numerical computations described in Section 4, we will take $\alpha=1$, $\tau_{\boldsymbol{P}}=1/2$, $\tau_{\boldsymbol{u}}=h\,\bar{l}(\Omega_0)$ and $c_N=1$. In summary, we obtain the SBM variational formulation:

$$\begin{aligned}&\textit{Find}\;[\boldsymbol{u}^h,\boldsymbol{P}^h]\in\mathbb{V}^h_{\boldsymbol{u}}(\tilde{\Omega}_0^h)\times\mathbb{V}^h_{\boldsymbol{P}}(\tilde{\Omega}_0^h)\;\textit{such that},\;\forall[\boldsymbol{\phi}^h,\boldsymbol{\psi}^h]\in\mathbb{V}^h_{\boldsymbol{u}}(\tilde{\Omega}_0^h)\times\mathbb{V}^h_{\boldsymbol{P}}(\tilde{\Omega}_0^h),\\&\mathscr{B}_{\text{SBM}}^{[\tilde{\Omega}_0^h]}([\boldsymbol{u}^h,\boldsymbol{P}^h];[\boldsymbol{\phi}^h,\boldsymbol{\psi}^h])=\mathscr{L}_{\text{SBM}}^{[\tilde{\Omega}_0^h]}([\boldsymbol{\phi}^h,\boldsymbol{\psi}^h])\,,\end{aligned} \tag{28a}$$

where

$$\begin{aligned}\mathscr{B}_{\text{SBM}}^{[\tilde{\Omega}_0^h]}([\boldsymbol{u}^h,\boldsymbol{P}^h];[\boldsymbol{\phi}^h,\boldsymbol{\psi}^h])=\;&\mathscr{B}_{\tilde{\Omega}_0^h}([\boldsymbol{u}^h,\boldsymbol{P}^h];[\boldsymbol{\phi}^h,\boldsymbol{\psi}^h])+\mathscr{B}_{s;\tilde{\Omega}_0^h}([\boldsymbol{u}^h,\boldsymbol{P}^h];[\boldsymbol{\phi}^h,\boldsymbol{\psi}^h])+\mathscr{B}_{\tilde{\Gamma}^h_{0,D}}([\boldsymbol{u}^h,\boldsymbol{P}^h];[\boldsymbol{\phi}^h,\boldsymbol{\psi}^h])\\&+\mathscr{B}_{\tilde{\Gamma}^h_{0,N}}([\boldsymbol{u}^h,\boldsymbol{P}^h];[\boldsymbol{\phi}^h,\boldsymbol{\psi}^h])\,,\end{aligned} \tag{28b}$$

$$\mathscr{L}_{\text{SBM}}^{[\tilde{\Omega}_0^h]}([\boldsymbol{\phi}^h,\boldsymbol{\psi}^h])=\mathscr{L}_{\tilde{\Omega}_0^h}([\boldsymbol{\phi}^h,\boldsymbol{\psi}^h])+\mathscr{L}_{s;\tilde{\Omega}_0^h}([\boldsymbol{\phi}^h,\boldsymbol{\psi}^h])+\mathscr{L}_{\tilde{\Gamma}^h_{0,D}}([\boldsymbol{\phi}^h,\boldsymbol{\psi}^h])+\mathscr{L}_{\tilde{\Gamma}^h_{0,N}}([\boldsymbol{\phi}^h,\boldsymbol{\psi}^h])\,, \tag{28c}$$

with

$$\mathscr{B}_{\tilde{\Omega}_0^h}([\boldsymbol{u}^h,\boldsymbol{P}^h];[\boldsymbol{\phi}^h,\boldsymbol{\psi}^h])=(\boldsymbol{P}^h,\nabla_{\boldsymbol{X}}\boldsymbol{\phi}^h)_{\tilde{\Omega}_0^h}+(\boldsymbol{P}^h-\boldsymbol{P}(\boldsymbol{u}^h),\boldsymbol{\psi}^h)_{\tilde{\Omega}_0^h}\,, \tag{28d}$$

$$\mathscr{B}_{s;\tilde{\Omega}_0^h}([\boldsymbol{u}^h,\boldsymbol{P}^h];[\boldsymbol{\phi}^h,\boldsymbol{\psi}^h])=-\tau_{\boldsymbol{P}}(\boldsymbol{P}^h-\boldsymbol{P}(\boldsymbol{u}^h),\boldsymbol{\psi}^h+\nabla_{\boldsymbol{X}}\boldsymbol{\phi}^h)_{\tilde{\Omega}_0^h}+\tau_{\boldsymbol{u}}(\nabla_{\boldsymbol{X}}\cdot\boldsymbol{P}^h\,,\,\nabla_{\boldsymbol{X}}\cdot\boldsymbol{\psi}^h)_{\tilde{\Omega}_0^h}\,, \tag{28e}$$

$$\begin{aligned}\mathscr{B}_{\tilde{\Gamma}^h_{0,D}}([\boldsymbol{u}^h,\boldsymbol{P}^h];[\boldsymbol{\phi}^h,\boldsymbol{\psi}^h])=\;&-\langle\boldsymbol{P}^h\tilde{\boldsymbol{N}},\boldsymbol{\phi}^h\rangle_{\tilde{\Gamma}^h_{0,D}}+\langle\mathcal{S}_D^h\boldsymbol{u}^h,(\mathcal{C}(\boldsymbol{u}^h)\,\boldsymbol{\psi}^h)\tilde{\boldsymbol{N}}\rangle_{\tilde{\Gamma}^h_{0,D}}\\&+\alpha\,\langle\|\mathcal{C}_{\text{vol}}(\boldsymbol{u}^h)\|\,h_\perp^{-1}(\tilde{\boldsymbol{N}}\otimes\tilde{\boldsymbol{N}})\,\mathcal{S}_D^h\boldsymbol{\phi}^h\,,\,\mathcal{S}_D^h\boldsymbol{u}^h\rangle_{\tilde{\Gamma}^h_{0,D}}\\&+\alpha\,\langle\|\mathcal{C}_{\text{dev}}(\boldsymbol{u}^h)\|\,h_\perp^{-1}(\boldsymbol{I}-\tilde{\boldsymbol{N}}\otimes\tilde{\boldsymbol{N}})\,\mathcal{S}_D^h\boldsymbol{\phi}^h\,,\,\mathcal{S}_D^h\boldsymbol{u}^h\rangle_{\tilde{\Gamma}^h_{0,D}}\,,\end{aligned} \tag{28f}$$

$$\mathscr{B}_{\tilde{\Gamma}^h_{0,N}}([\boldsymbol{u}^h,\boldsymbol{P}^h];[\boldsymbol{\phi}^h,\boldsymbol{\psi}^h])=\langle(\boldsymbol{N}\cdot\tilde{\boldsymbol{N}})(\mathcal{S}_N^h\boldsymbol{P}^h)\boldsymbol{N}-\boldsymbol{P}^h\tilde{\boldsymbol{N}},\boldsymbol{\phi}^h\rangle_{\tilde{\Gamma}^h_{0,N}}+\langle\tau_N(\mathcal{S}_N^h\boldsymbol{P}^h)\boldsymbol{N},(\tilde{\boldsymbol{N}}\cdot\boldsymbol{N})^2(\mathcal{S}_N^h\boldsymbol{\psi}^h)\boldsymbol{N}\rangle_{\tilde{\Gamma}^h_{0,N}}\,, \tag{28g}$$

$$\mathscr{L}_{\tilde{\Omega}_0^h}([\boldsymbol{\phi}^h,\boldsymbol{\psi}^h])=(\rho_0\boldsymbol{b},\boldsymbol{\phi}^h)_{\tilde{\Omega}_0^h}\,, \tag{28h}$$

$$\mathscr{L}_{s;\tilde{\Omega}_0^h}([\boldsymbol{\phi}^h,\boldsymbol{\psi}^h])=-\tau_{\boldsymbol{u}}(\rho_0\boldsymbol{b},\nabla_{\boldsymbol{X}}\cdot\boldsymbol{\psi}^h)_{\tilde{\Omega}_0^h}\,, \tag{28i}$$

$$\begin{aligned}\mathscr{L}_{\tilde{\Gamma}^h_{0,D}}([\boldsymbol{\phi}^h,\boldsymbol{\psi}^h])=\;&\langle\boldsymbol{u}_D,(\mathcal{C}(\boldsymbol{u}^h)\,\boldsymbol{\psi}^h)\tilde{\boldsymbol{N}}\rangle_{\tilde{\Gamma}^h_{0,D}}+\alpha\,\langle\|\mathcal{C}_{\text{vol}}(\boldsymbol{u}^h)\|\,h_\perp^{-1}\boldsymbol{u}_D\,,(\tilde{\boldsymbol{N}}\otimes\tilde{\boldsymbol{N}})\,\mathcal{S}_D^h\boldsymbol{\phi}^h\rangle_{\tilde{\Gamma}^h_{0,D}}\\&+\alpha\,\langle\|\mathcal{C}_{\text{dev}}(\boldsymbol{u}^h)\|\,h_\perp^{-1}\boldsymbol{u}_D\,(\boldsymbol{I}-\tilde{\boldsymbol{N}}\otimes\tilde{\boldsymbol{N}})\,\mathcal{S}_D^h\boldsymbol{\phi}^h\rangle_{\tilde{\Gamma}^h_{0,D}}\,,\end{aligned} \tag{28j}$$

$$\mathscr{L}_{\tilde{\Gamma}^h_{0,N}}([\boldsymbol{\phi}^h,\boldsymbol{\psi}^h])=\langle\boldsymbol{T}_N,(\boldsymbol{N}\cdot\tilde{\boldsymbol{N}})\boldsymbol{\phi}^h\rangle_{\tilde{\Gamma}^h_{0,N}}+\langle\tau_N\boldsymbol{T}_N,(\tilde{\boldsymbol{N}}\cdot\boldsymbol{N})^2(\mathcal{S}_N^h\boldsymbol{\psi}^h)\boldsymbol{N}\rangle_{\tilde{\Gamma}^h_{0,N}}\,. \tag{28k}$$

3.4. An efficient variational implementation of the Shifted Boundary Method

Solving the mixed form of the linear elasticity equations is often undesirable due to the increase in the number of degrees of freedom and thus the associated computational cost. At the same time, a primal formulation with Neumann boundary conditions

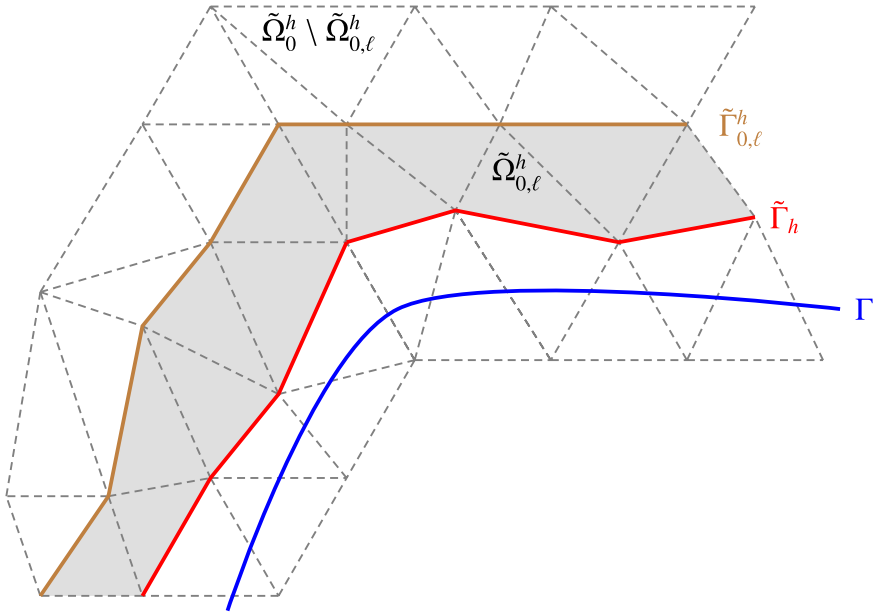

Fig. 4. The true boundary Γ_0 (blue), the surrogate boundary $\tilde{\Gamma}_0^h$ (red), the set of elements with one node on the surrogate boundary $\tilde{\Omega}_{0,\ell}^h$ (gray), the set of elements with no nodes on surrogate boundary $\tilde{\Omega}_0^h \setminus \tilde{\Omega}_{0,\ell}^h$, and the interface $\tilde{\Gamma}_{0,\ell}^h$ (brown) between $\tilde{\Omega}_{0,\ell}^h$ and $\tilde{\Omega}_0^h \setminus \tilde{\Omega}_{0,\ell}^h$. (For interpretation of the references to color in this figure legend, the reader is referred to the web version of this article.)

and $\boldsymbol{u}^h \in \mathbb{V}_{\boldsymbol{u}}^h(\tilde{\Omega}_0^h)$ would lead to a first-order accurate method, since, for example, the second-order derivatives of $\boldsymbol{u}^h$, required by the Taylor expansion of the first Piola–Kirchhoff stress, vanish at any quadrature point for tetrahedral finite elements.

This section introduces a strategy that significantly reduces the computational burden of solving the mixed system without jeopardizing the accuracy of the finite element displacement solution $\boldsymbol{u}^h$. The key idea is to apply the mixed formulation only the layer of elements that have at least one node on the surrogate boundary. Roughly speaking, the thickness of the layer we are considering is one element. In [32], it was shown that this strategy is effective for simulations of linear elasticity, and that further increasing the thickness of the layer of elements does not substantially improve the numerical solution.

Recalling the definitions of $\tilde{\Omega}_0^h$ and $\tilde{\Gamma}_0^h$ in Section 3.1, we define $\tilde{\Omega}_{0,\ell}^h$ as the set of elements $\tilde{T} \subset \tilde{\Omega}_0^h$ with at least one node on $\tilde{\Gamma}_0^h$ (see Fig. 4), that is,

$$\tilde{\Omega}_{0,\ell}^h = \{\tilde{T} \subset \tilde{\Omega}_0^h \,:\, \tilde{T} \cap \tilde{\Gamma}_0^h \neq \emptyset\}. \tag{29}$$

The main idea is to solve a mixed variational formulation only on $\tilde{\Omega}_{0,\ell}^h$ while on the rest of the computational domain, namely $\tilde{\Omega}_0^h \setminus \tilde{\Omega}_{0,\ell}^h$, a primal formulation of (1) where only the displacement $\boldsymbol{u}^h$ is solved for as unknown. The governing equations in $\tilde{\Omega}_0^h \setminus \tilde{\Omega}_{0,\ell}^h$ can thus be expressed as follows:

$$-\nabla \cdot (\boldsymbol{P}(\boldsymbol{u}^h)) = \rho_0 \boldsymbol{b}\,, \qquad \text{in } \tilde{\Omega}_0^h \setminus \tilde{\Omega}_{0,\ell}^h\,, \tag{30a}$$

$$\boldsymbol{P}(\boldsymbol{u}^h)^+ \boldsymbol{N}^+ + \boldsymbol{P}^{h,-} \boldsymbol{N}^- = \boldsymbol{0}\,, \qquad \text{on } \tilde{\Gamma}_{0,\ell}^h\,, \tag{30b}$$

where the "+" and "−" signs refer to the primal ($\tilde{\Omega}_0^h \setminus \tilde{\Omega}_{0,\ell}^h$) and mixed ($\tilde{\Omega}_{0,\ell}^h$) sides of the domain, respectively. Eq. (30b) enforces continuity of the normal component of the stress across the interface $\tilde{\Gamma}_{0,\ell}^h = \partial \tilde{\Omega}_{0,\ell}^h \setminus \tilde{\Gamma}_0^h$. Obviously, the displacement field $\boldsymbol{u}^h$ is continuous over $\tilde{\Omega}_0^h$ and in particular across $\tilde{\Gamma}_{0,\ell}^h$. Defining the discrete test functions as $[\boldsymbol{\phi}^h, \boldsymbol{\psi}^h] \in \mathbb{V}_{\boldsymbol{u}}^h(\tilde{\Omega}_0^h) \times \mathbb{V}_{\boldsymbol{P}}^h(\tilde{\Omega}_{0,\ell}^h)$, multiplying (30a) by $\boldsymbol{\phi}^h|_{\tilde{\Omega}^h \setminus \tilde{\Omega}_{0,\ell}^h}$ and integrating by parts gives

$$0 = (\boldsymbol{P}(\boldsymbol{u}^h)\,,\, \nabla_{\boldsymbol{X}} \boldsymbol{\phi}^h)_{\tilde{\Omega}_0^h \setminus \tilde{\Omega}_{0,\ell}^h} - \langle \boldsymbol{P}(\boldsymbol{u}^h)^+ \boldsymbol{N}^+, \boldsymbol{\phi}^h \rangle_{\tilde{\Gamma}_{0,\ell}^h} = (\rho_0 \boldsymbol{b}, \boldsymbol{\phi}^h)_{\tilde{\Omega}_0^h \setminus \tilde{\Omega}_{0,\ell}^h}. \tag{31}$$

Consider now the restriction of (1a) and (1b) to $\tilde{\Omega}_{0,\ell}^h$, multiplied by $\boldsymbol{\phi}^h_{|\tilde{\Omega}_{0,\ell}^h}$ and $\boldsymbol{\psi}^h$, respectively. Following analogous derivations to the ones outlined in Section 3.3, we obtain

$$\mathscr{B}_{\text{SBM}}^{[\tilde{\Omega}_{0,\ell}^h]}([\boldsymbol{u}^h, \boldsymbol{P}^h]; [\boldsymbol{\phi}^h, \boldsymbol{\psi}^h]) - \langle \boldsymbol{P}^{h,-} \boldsymbol{N}^-\,,\, \boldsymbol{\phi}^h \rangle_{\tilde{\Gamma}_{0,\ell}^h} = \mathscr{L}_{\text{SBM}}^{[\tilde{\Omega}_{0,\ell}^h]}([\boldsymbol{\phi}^h, \boldsymbol{\psi}^h]). \tag{32}$$

Adding (31) to (32) and enforcing (30b) gives the following final variational form:

$$\textit{Find } [\boldsymbol{u}^h, \boldsymbol{P}^h] \in \mathbb{V}_{\boldsymbol{u}}^h(\tilde{\Omega}_0^h) \times \mathbb{V}_{\boldsymbol{P}}^h(\tilde{\Omega}_{0,\ell}^h) \textit{ such that, } \forall [\boldsymbol{\phi}^h, \boldsymbol{\psi}^h] \in \mathbb{V}_{\boldsymbol{u}}^h(\tilde{\Omega}_0^h) \times \mathbb{V}_{\boldsymbol{P}}^h(\tilde{\Omega}_{0,\ell}^h),$$

$$\mathscr{B}_{\text{SBM}}([\boldsymbol{u}^h, \boldsymbol{P}^h]; [\boldsymbol{\phi}^h, \boldsymbol{\psi}^h]) = \mathscr{L}_{\text{SBM}}([\boldsymbol{\phi}^h, \boldsymbol{\psi}^h]) \,, \tag{33a}$$

where

$$\mathscr{B}_{\text{SBM}}([\boldsymbol{u}^h, \boldsymbol{P}^h]; [\boldsymbol{\phi}^h, \boldsymbol{\psi}^h]) = (\boldsymbol{P}(\boldsymbol{u}^h), \nabla_{\boldsymbol{X}} \boldsymbol{\phi}^h)_{\tilde{\Omega}^h_0 \setminus \tilde{\Omega}^h_{0,\ell}} + \mathscr{B}^{[\tilde{\Omega}^h_{0,\ell}]}_{\text{SBM}}([\boldsymbol{u}^h, \boldsymbol{P}^h]; [\boldsymbol{\phi}^h, \boldsymbol{\psi}^h]) \,, \tag{33b}$$

$$\mathscr{L}_{\text{SBM}}([\boldsymbol{\phi}^h, \boldsymbol{\psi}^h]) = (\rho_0 \boldsymbol{b}, \boldsymbol{\phi}^h)_{\tilde{\Omega}^h \setminus \tilde{\Omega}^h_{0,\ell}} + \mathscr{L}^{[\tilde{\Omega}^h_{0,\ell}]}_{\text{SBM}}([\boldsymbol{\phi}^h, \boldsymbol{\psi}^h]) \,. \tag{33c}$$

Remark 3. Because formulation (33) restricts the mixed variational formulation to a small layer of elements $\tilde{\Omega}^h_{0,\ell}$ near the boundary $\tilde{\Gamma}^h_0$, it can be interpreted as a *gradient reconstruction technique*, built to ensure optimal error convergence.

4. Numerical experiments

In the simulations presented next, unless otherwise specified, we set the parameters $\alpha = 1$, $\tau_{\boldsymbol{P}} = 1/2$, $\tau_{\boldsymbol{u}} = h\,\bar{l}(\Omega_0)$ and $c_N = 1$. These choices were already presented in Section 3.3. All SBM simulations were performed with the efficient formulation (33), which from now on will be simply referred to as the SBM formulation. The algebraic system of equations is solved using the Additive Schwarz domain decomposer within the Trilinos Software Project [59] lead by Sandia National Laboratories. To facilitate the convergence of the Newton solver, the following adaptive load step control strategy is adopted: given a current load increment, the subsequent load increment is increased by 25%, unless the Newton–Raphson solver fails to converge, in which case the load increment is cut in half and the last failed step is recomputed. This strategy is recursively applied starting with an initial load increment.

4.1. Post-processing of stress measures

In all tests, the volumetric component of the Cauchy stress (the pressure $p = \text{tr}(\boldsymbol{\sigma})/n_d$) and the square root of the von Mises stress ($\sqrt{J_2}$) are sampled as stress measures. The von Mises stress is nominally defined as

$$J_2 = (1/2)\,\boldsymbol{\sigma}_{\text{dev}} : \boldsymbol{\sigma}_{\text{dev}} \tag{34}$$

where $\boldsymbol{\sigma}_{\text{dev}} = \boldsymbol{\sigma} - p\boldsymbol{I}$ is the deviatoric component of the Cauchy stress. The Cauchy stress is post-processed from the Piola stress using the deformation gradient $\boldsymbol{F}(\boldsymbol{u})$ and Jacobian determinant $J(\boldsymbol{u})$, obtained from the displacement gradients with respect to the reference (original) configuration.

Typically, the above stress measures are calculated and plotted over the surrogate domain $\tilde{\Omega}^h$ or surrogate boundary $\tilde{\Gamma}^h$, both in the current configuration. However, it is also important in the engineering practice to sample the stress over the surface of the true boundary or the gap between the surrogate and true boundary. This is accomplished by first evaluating the above stress measures over the element faces lying on the surrogate boundary and then extrapolating their values to the true boundary as constants. Since the overall SBM formulation is second-order accurate, this strategy is simple and compatible with the overall order of accuracy of the method. There is no need for more sophisticated strategies since the overall stress accuracy is limited to first order (similar to the body-fitted case).

The evaluation of the stress in the gap between the surrogate and the true boundary is similar. Consider an element face lying on the surrogate boundary, and the generalized prism (in two or three dimensions) obtained by projecting its nodes to the true boundary along the nodal distance vectors $\boldsymbol{d}$. The stress measures are extrapolated as constant inside the prism. Fig. 5 shows a two-dimensional sketch, where the face $\tilde{B}\tilde{A}$ lies on the surrogate boundary and the generalized prism is the quadrilateral $BA\tilde{A}\tilde{B}$. The stress measures are evaluated on the face $\tilde{B}\tilde{A}$ and then extrapolated as constants inside the prism, all the way to the face BA on the true boundary. The three-dimensional case is similar.

4.2. Post-processing of the deformation of the true geometry

Equally important is the post-processing of the deformation of the true geometry, which can be accomplished with the following strategy. Let us consider again the two-dimensional sketch in Fig. 5: node $\tilde{B}$ occupies the (initial) position $\tilde{\boldsymbol{X}}_{\tilde{B}}$ on the surrogate boundary, and we can compute, with the help of distance vector $\boldsymbol{D}$ (again in the original configuration), the position $\boldsymbol{X}_B$ of the corresponding point B on the true boundary:

$$\boldsymbol{X}_B = \tilde{\boldsymbol{X}}_{\tilde{B}} + \boldsymbol{D}(\tilde{\boldsymbol{X}}_{\tilde{B}}). \tag{35}$$

To compute the displacement $\boldsymbol{u}_{|B}$ of point B, an average gradient is computed over all the elements that share node $\tilde{B}$ and the displacement at B is extrapolated using Taylor expansions centered at $\tilde{\boldsymbol{X}}_{\tilde{B}}$:

$$\boldsymbol{u}_{|B} = \boldsymbol{u}_{|\tilde{B}} + \left(\frac{1}{n_{\tilde{B}}} \sum_{i=1}^{n_{\tilde{B}}} (\nabla_{\boldsymbol{X}} \boldsymbol{u})^{(i)}_{|\tilde{B}} \right) \boldsymbol{D} \,, \tag{36}$$

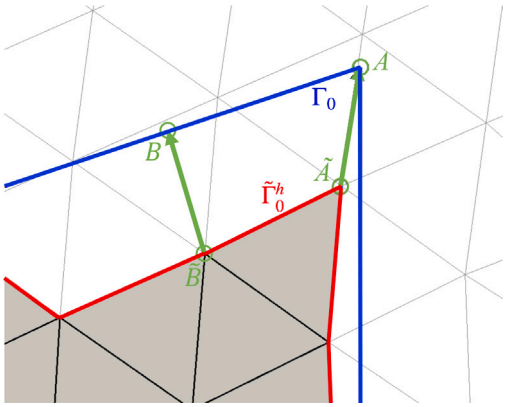

Fig. 5. Sketch of the reconstruction of the geometry of the true boundary from the geometry of the surrogate boundary and the distance vector function $\boldsymbol{d}$. The face connecting nodes $\tilde{A}$ and $\tilde{B}$, on the surrogate boundary, is mapped by the distance map to the face connecting the corresponding points A and B, on the true boundary.

where $n_{\tilde{B}}$ is the total number of elements in $\tilde{\Omega}_0^h$ attached to node $\tilde{B}$, and $(\nabla_{\boldsymbol{X}}\boldsymbol{u})^{(i)}_{|\tilde{B}}$ is the gradient of the displacement in element i evaluated at $\tilde{B}$. This technique can be applied to any node on the surrogate boundary. The position in the current configuration of points on the true boundary (corresponding to nodes on the surrogate boundary) can then be computed combining (35) and (36):

$$\boldsymbol{x}_{|B} = \boldsymbol{X}_{|B} + \boldsymbol{u}_{|B} = \tilde{\boldsymbol{X}}_{\tilde{B}} + \boldsymbol{D}(\tilde{\boldsymbol{X}}_{\tilde{B}}) + \boldsymbol{u}_{|\tilde{B}} + \left(\frac{1}{n_{\tilde{B}}} \sum_{i=1}^{n_{\tilde{B}}} (\nabla_{\boldsymbol{X}}\boldsymbol{u})^{(i)}_{|\tilde{B}} \right) \boldsymbol{D} \, . \tag{37}$$

The same ideas can be extended to the three-dimensional case.

4.3. Two-dimensional Cook's membrane test

To test the SBM formulation under a combined shear/bending behavior, we adapted the Cook's membrane test [42,60]. We consider a state of plane strain with a bulk modulus $\kappa = 208.33$ GPa and a shear modulus $\mu = 96.15$ GPa, which imply a compressible response of the material. The geometry is presented in Fig. 6(a) with a leading dimension $\bar{l}(\Omega_0) = 60$ m. A homogeneous Dirichlet boundary condition on the displacement is applied to the left side of the boundary (depicted in green, in Fig. 6(b)). A uniform tangential traction of $\boldsymbol{t}_N = 6.25$ GPa (Neumann boundary condition) is enforced on the right side, depicted in blue in Fig. 6(b). Traction-free (Neumann) boundary conditions are imposed on the top and bottom boundaries (in red and brown, in Fig. 6(b)).

Fig. 6(c) depicts the surrogate domain $\tilde{\Omega}_0^h$ and the layer of elements $\tilde{\Omega}_{0,\ell}^h$, for a coarse grid such that $\tilde{\Omega}_0^h \subset \Omega_0$ and Fig. 6(d) displays how each of the sides of the true boundary maps to a corresponding sideset of the surrogate boundary (using again the color scheme green–red–blue–brown). We refer to this configuration as a domain Ω_0 with *enclosed surrogate* $\tilde{\Omega}_0^h$.

Fig. 6(e) depicts instead the surrogate domain $\tilde{\Omega}_0^h$ and the layer of elements $\tilde{\Omega}_{0,\ell}^h$, for a coarse grid such that the domain Ω_0 is contained in the surrogate domain, namely $\Omega_0 \subset \tilde{\Omega}_0^h$. We refer to this configuration as a domain Ω_0 with *enclosing surrogate* $\tilde{\Omega}_0^h$. Numerical experiments show that the SBM is not particularly sensitive to the location of the surrogate boundary, as long as its distance to the true boundary is of the same order of the grid size.

Fig. 6(f) displays how each of the sides of the true boundary maps to a corresponding sideset of the surrogate boundary (using again the color scheme green–red–blue–brown).

For the SBM simulations, we adopted seven levels of refinement of a structured grid of the type shown in Figs. 6(c)–6(f). The SBM simulations are compared against a primal body-fitted formulation whereby the Dirichlet boundary conditions are enforced strongly. Similar refinements were considered for the body-fitted FEM, for grids of the type depicted in Fig. 6(b).

The convergence of the tip displacement of the Cook's membrane (i.e., the displacement of point A in Fig. 7(a)) is shown in Fig. 7(b) for the SBM formulation (33) with inner and enclosing surrogate boundary choices, the body-fitted formulation, and a reference solution obtained solving the body-fitted primal formulation on the finest grid.

To locate the node on the surrogate boundary corresponding to the tip of the Cook's membrane, we first find the surrogate node $\tilde{A}$ (corresponding to the tip node A) as the node lying at the intersection between the two sidesets associated with the vertical traction and traction-free conditions (see Fig. 7(a)), and then we extrapolate the solution's displacement from $\tilde{A}$ to A according to a formula analogous to (36).

Fig. 7(b) plots the vertical displacement of $\boldsymbol{u}|_A$ and the results show that the SBM formulation is at least as accurate as its primal body-fitted counterpart for comparable mesh sizes. Note that the SBM solution obtained with the enclosed surrogate domain strategy is more accurate than the body-fitted FEM on the four coarsest grids.

Figs. 8 and 9 show the SBM numerical solution for the four finest levels of refinement of the embedded grids using the enclosed and enclosing surrogates, respectively. In particular, the first row of plots shows the magnitude of the displacement field, the second

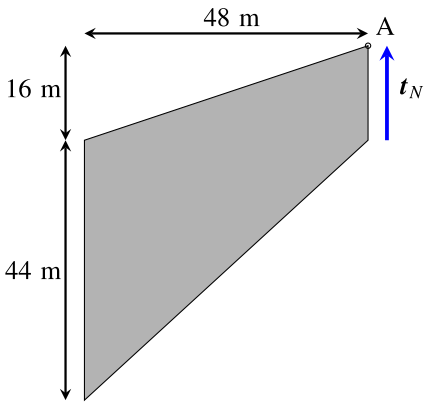

(a) The domain Ω_0 and the traction force t_N.

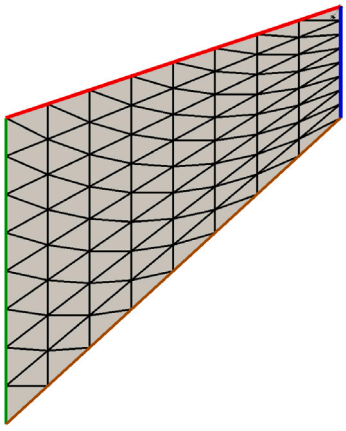

(b) A body-fitted grid and the four sides of $\Gamma_0 = \partial\Omega_0$.

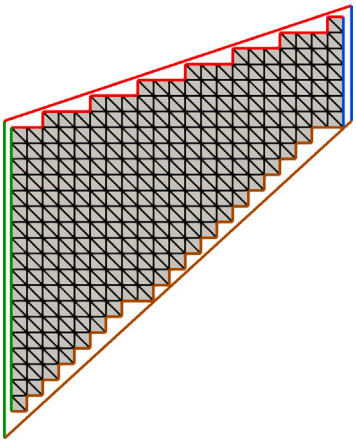

(c) An enclosed surrogate domain $\tilde{\Omega}_0^h \subset \Omega_0$: the mapping of boundary conditions on the sides of $\tilde{\Omega}_0^h$.

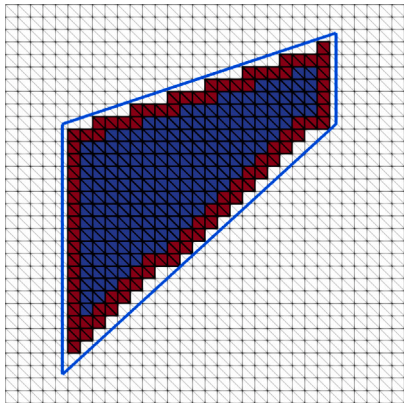

(d) An enclosed surrogate domain $\tilde{\Omega}_0^h \subset \Omega_0$: $\tilde{\Omega}_{0,\ell}^h$ (red), $\tilde{\Omega}_0^h \setminus \tilde{\Omega}_{0,\ell}^h$ (blue) and Γ_0 (blue outline).

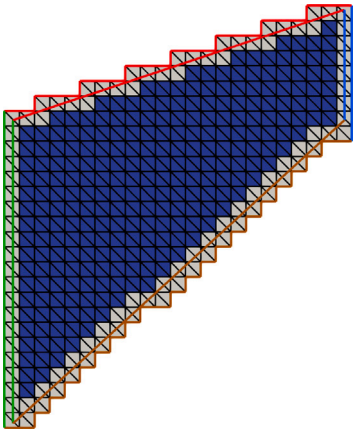

(e) An enclosing surrogate domain $\Omega_0 \subset \tilde{\Omega}_0^h$: the mapping of boundary conditions on the sides of $\tilde{\Omega}_0^h$.

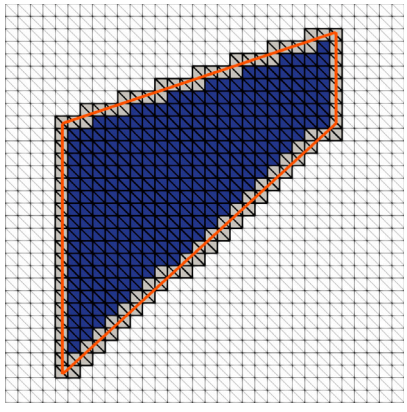

(f) An enclosing surrogate domain $\Omega_0 \subset \tilde{\Omega}_0^h$: $\tilde{\Omega}_{0,\ell}^h$ (gray), $\tilde{\Omega}^h \setminus \tilde{\Omega}_{0,\ell}^h$ (blue) and Γ_0 (red outline).

Fig. 6. Setup of the Cook's membrane problem, with depiction of the true domain Ω, the surrogate domain $\tilde{\Omega}_0^h$, the true boundary Γ_0, the surrogate boundary $\tilde{\Gamma}_0^h$, and the layer of surrogate boundary elements $\tilde{\Omega}_{0,\ell}^h$. The correspondence between the surrogate and the true sides of the boundary is expressed with different colors, using the color scheme green–red–blue–brown. The plots in the middle row refer to an enclosed surrogate boundary, $\tilde{\Omega}_0^h \subset \Omega_0$, while the plots on the bottom row refer to an enclosing surrogate boundary, $\Omega_0 \subset \tilde{\Omega}_0^h$. (For interpretation of the references to color in this figure legend, the reader is referred to the web version of this article.)

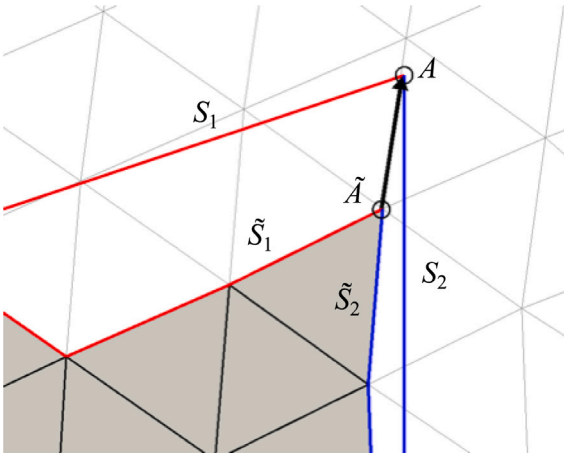

(a) Point A, at the top right corner of the Cook's membrane, and its corresponding surrogate node $\tilde{A}$, the sidesets S_1(red) and S_2(blue) on the true boundary and the corresponding surrogate sidesets $\tilde{S}_1$ and $\tilde{S}_2$ on the surrogate boundary.

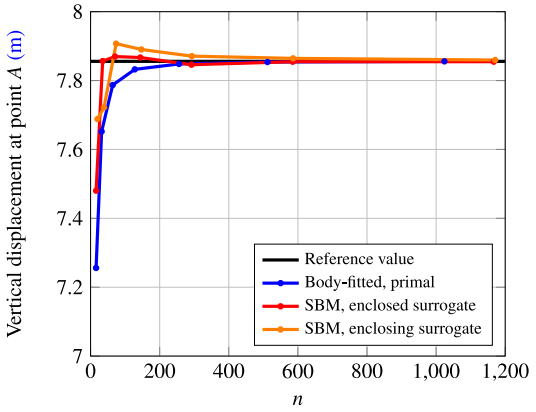

(b) Vertical displacement at point A, where n is the total number of edges along $S_1 \cup S_2$, for the primal body-fitted formulation, or the total number of edges along $\tilde{S}_1 \cup \tilde{S}_2$, for the SBM formulation. The red/orange curves correspond to the settings in Figure 6c/6e, respectively.

Fig. 7. Left: Point A at the tip of the true boundary (top right corner) and the corresponding surrogate node $\tilde{A}$. Right: plots of the vertical displacement at point A for a primal body-fitted formulation and the enhanced SBM formulation. In the case of the SBM, the displacement at A is estimated from the displacement at $\tilde{A}$ using (36) with $\tilde{B}$ and B replaced by $\tilde{A}$ and A, respectively. (For interpretation of the references to color in this figure legend, the reader is referred to the web version of this article.)

row of plots shows the volumetric stress (pressure), and the third row of plots shows the square root of the von Mises stress ($\sqrt{J_2}$). All these quantities are sampled on the surrogate domains.

In both the SBM and the body-fitted computations, the final deformed configuration is reached with 24 loading steps of the adaptive load control strategy described at the very beginning of Section 4. This indicates that there are no significant differences in computational cost between the SBM and body fitted computations in the nonlinear Cook's membrane test (see also [32] for an analysis of the SBM computational cost in the linear case).

4.4. Twisting of a three-dimensional beam

We consider next the twisting of a three-dimensional beam-like structure of square section. The beam is a parallelepiped of dimension 1 m × 1 m × 6 m as shown in Fig. 10(a), and we set $\bar{l}(\Omega_0) = 6$ m as the characteristic dimension of Ω_0.

We set the bulk modulus $\kappa = 929.45$ GPa and the shear modulus $\mu = 96.15$ GPa so that the nominal Poisson ratio is 0.45 (note that the Poisson ratio makes sense only in linear elasticity and that the finite elasticity model used here collapses to the equations of linear elasticity for infinitesimal displacements).

The body force $\boldsymbol{b}$ is zero and a Dirichlet condition

$$\boldsymbol{u} = \begin{Bmatrix} u_x \\ u_y \\ u_z \end{Bmatrix} = \begin{Bmatrix} x\cos(t\,\pi/6) - z\sin(t\,\pi/6) - x \\ 0 \\ x\sin(t\,\pi/6) + z\cos(t\,\pi/6) - z \end{Bmatrix} \text{ m} \tag{38}$$

is applied at the top boundary while the bottom boundary is clamped (homogeneous Dirichlet condition). The top boundary is progressively deformed adaptively increasing the load parameter t from 0 to 11. Traction free (homogeneous Neumann) boundary conditions are enforced at the remaining surfaces. To apply the SBM formulation (33), we immerse the domain Ω_0 in a background domain (shown in gray in Fig. 10(b)) and generate an enclosed surrogate domain $\tilde{\Omega}_0^h \subset \Omega_0$, colored in blue in Figs. 11(a) and 11(d) for a coarse and fine background grid, respectively.

Because of the lack of exact analytical solutions, an error convergence study is not feasible. As an alternative, Figs. 11(a) and 11(d) show, in transparent gray, the reconstruction of the true deformed boundary, obtained by applying formula (37) to all nodes on $\tilde{\Gamma}_0^h$, for a coarse and fine grid, respectively. In Figs. 11(b) and 11(e), we overlap the aforementioned reconstructed true boundaries (this time in blue) with their body-fitted counterparts (in gray), obtained from solving a primal formulation with strong Dirichlet boundary conditions, again for a coarse and a fine grid.

While the discrepancy between the SBM and body-fitted surface formulation is clear for the coarse grid (Fig. 11(c)), the SBM-reconstructed and body-fitted true boundary surfaces become almost indistinguishable in the case of the fine grid (Fig. 11(f)).

Next, we consider the case of an enclosing surrogate domain $\tilde{\Omega}_0^h$ (i.e., $\Omega_0 \subset \tilde{\Omega}_0^h$), which is shown in transparent gray in Figs. 12(a) and 12(d) for a coarse and fine background grid, respectively.

The number of elements for the coarse and fine background grids is chosen so that the total number of active elements for this enclosing surrogate domain is similar to the case of the enclosed surrogate domain discussed above.

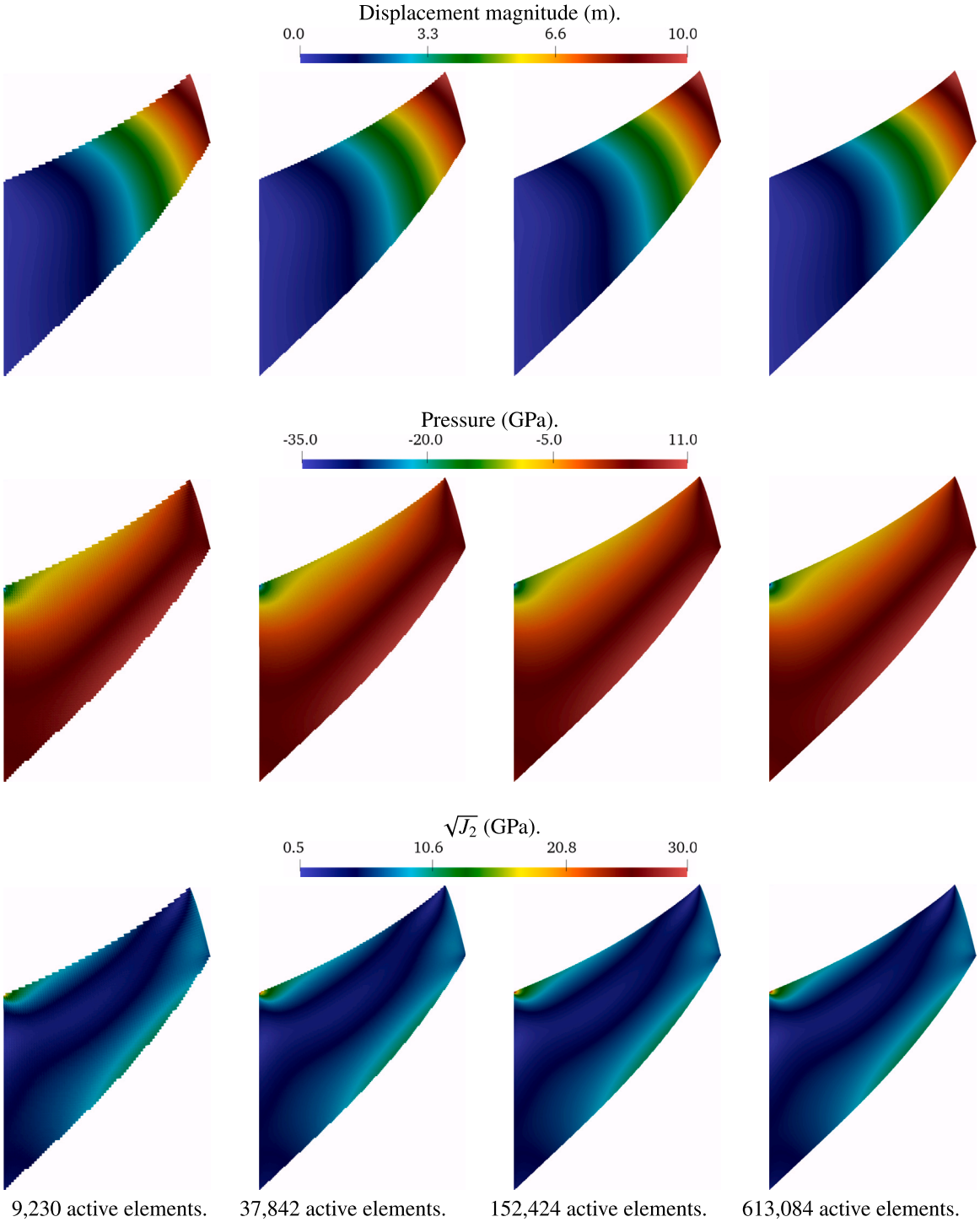

Fig. 8. Cook's membrane test: mesh refinement study for the SBM formulation with enclosed surrogate boundary ($\tilde{\Omega}_0^h \subset \Omega_0$). Contour plots of the displacement magnitude, the volumetric stress (pressure), and the square root of the von Mises stress ($\sqrt{J_2}$). The deformation is computed over the surrogate domains.

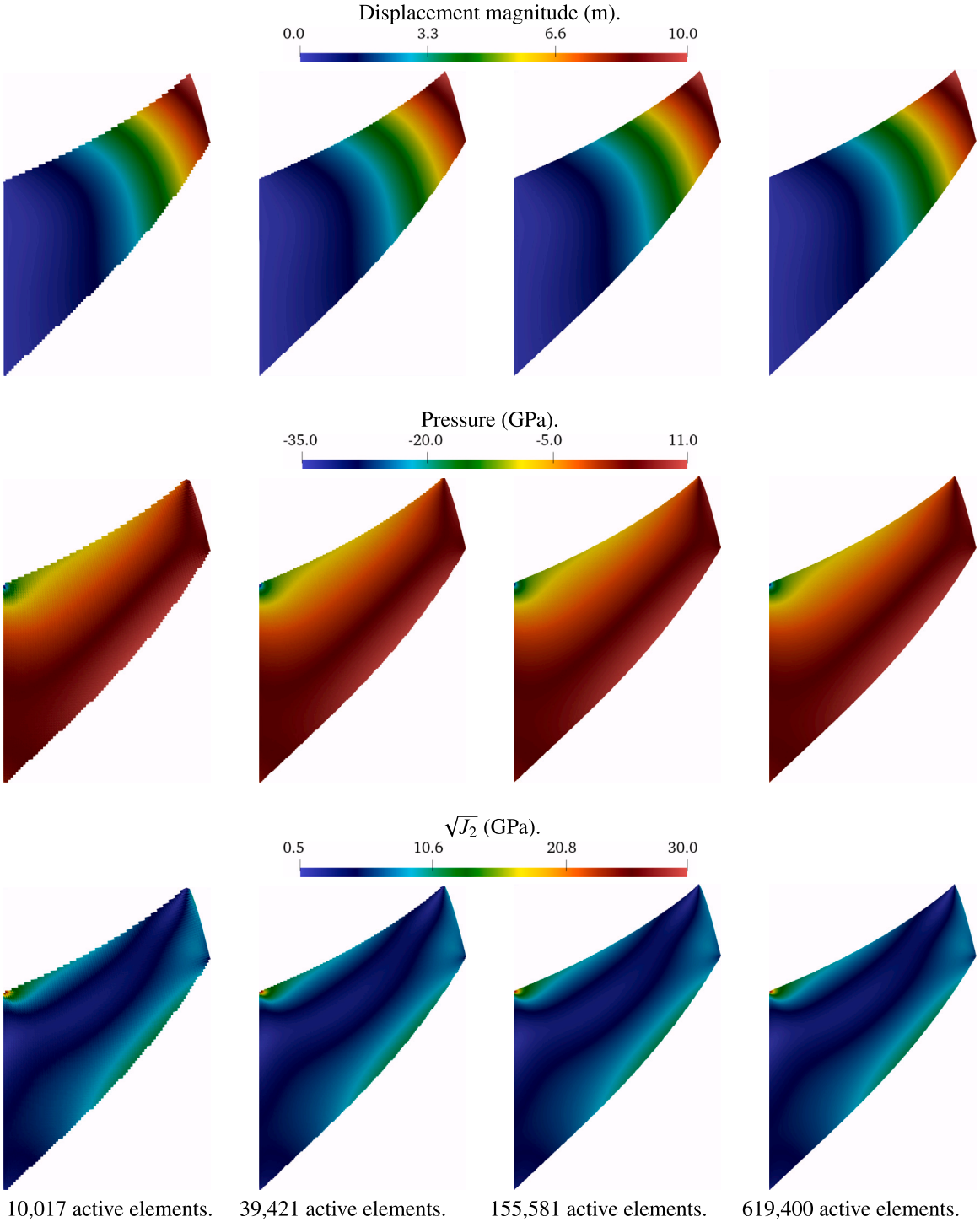

Fig. 9. Cook's membrane test: mesh refinement study for the SBM formulation with enclosing surrogate boundary ($\Omega_0 \subset \tilde{\Omega}_0^h$). Contour plots of the displacement magnitude, the volumetric stress (pressure), and the square root of the von Mises stress ($\sqrt{J_2}$). The deformation is computed over the surrogate domains.

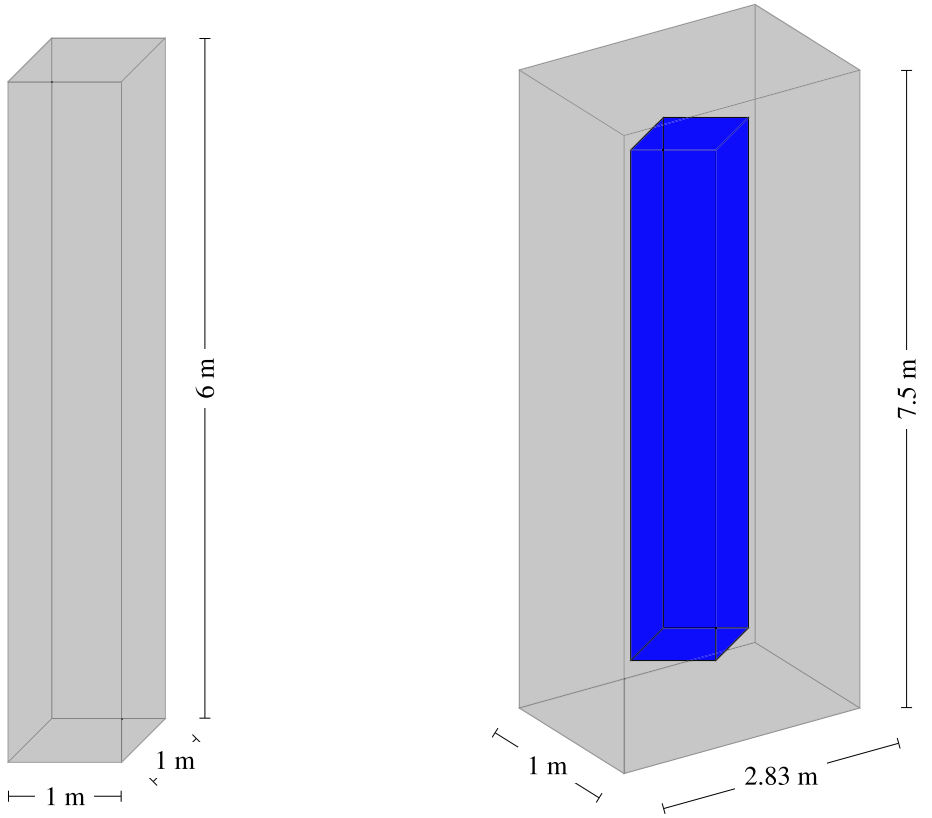

(a) Domain Ω and dimensions.

(b) Immersed domain Ω (blue) in a background geometry (gray).

Fig. 10. Twisting of a three-dimensional beam: The geometric setup of the beam in its initial configuration is shown in Fig. 10(a). The geometry and dimensions of the background computational domain where the true geometry is immersed is shown in Fig. 10(b). (For interpretation of the references to color in this figure legend, the reader is referred to the web version of this article.)

Table 1
Twisting of a three-dimensional beam: Initial load step and number of load steps for the SBM and body-fitted formulations.

Formulation	No. elements	No. active elements	Initial load step	No. loading steps
SBM ($\tilde{\Omega}_0^h \subset \Omega_0$)	25,150	1731	0.1	23
	1,105,763	140,617	0.1	59
SBM ($\Omega_0 \subset \tilde{\Omega}_0^h$)	5658	2040	0.1	24
	641,390	143,854	0.1	76
Body-fitted	1940	1940	0.1	28
	135,831	135,831	0.05	158

We reconstruct the true deformed surface according to formula (37) applied to all nodes on $\tilde{\Gamma}_0^h$ and color it in blue as shown in 12(a) and 12(d) for a coarse and fine grid respectively. In Figs. 12(b) and 12(e), we overlap the aforementioned reconstructed true boundaries (blue) with their body-fitted counterparts (gray), again for a coarse and a fine grid. Also in this case, the discrepancies between the SBM and the body-fitted computations are visible for the coarse grids (Fig. 12(c)) and negligible for the fine grids (Fig. 12(f)).

Fig. 13 shows the SBM numerical solutions for both the enclosed surrogate domain ($\tilde{\Omega}_0^h \subset \Omega_0$) and the enclosing surrogate domain ($\tilde{\Omega}_0^h \subset \Omega_0$), computed with the finest respective grids. In particular, the first of the three columns of plots shows the magnitude of the displacement field, the second the pressure, and the third the square root of the von Mises stress ($\sqrt{J_2}$). The first row refers to the enclosed surrogate case and the second row to the enclosing surrogate case. Both the displacement and stress fields are stable, smooth and free from spurious oscillations.

The pressure and square root of the von Mises stress ($\sqrt{J_2}$) on the body-fitted simulation and reconstructed true boundaries, for both the enclosed surrogate domain ($\tilde{\Omega}_0^h \subset \Omega_0$) and the enclosing surrogate domain ($\tilde{\Omega}_0^h \subset \Omega_0$), are shown in Fig. 14 computed with the finest respective grids. The first row of plots shows the pressure, the second row of plots shows the square root of the von Mises stress ($\sqrt{J_2}$), the first column refers to the body-fitted simulation, the second column refers to the enclosed surrogate SBM, and the third column refers to the enclosing surrogate SBM. Visually inspecting the results, the SBM simulations match closely

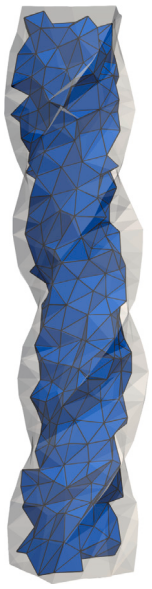

(a) Coarse grid: the surrogate boundary (blue) and the SBM-reconstructed true boundary (gray).

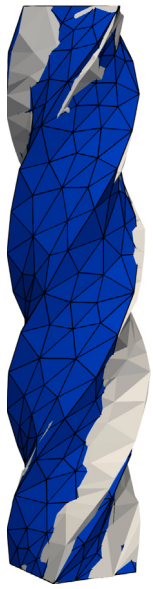

(b) Course grid: the boundary of a body-fitted computation (blue) and the SBM-reconstructed true boundary (gray).

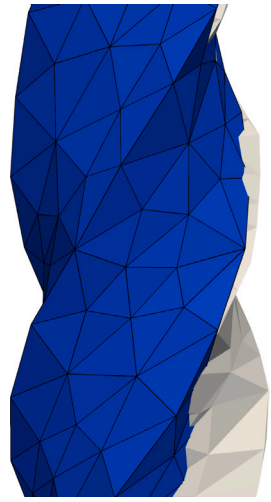

(c) Zoomed view of Figure 11b.

(d) Fine grid: the surrogate boundary (blue) and SBM-reconstructed true boundary (gray).

(e) Fine grid: the boundary of a body-fitted computation (blue) and the SBM-reconstructed true boundary (gray).

(f) Zoomed view of Figure 11e.

Fig. 11. Twisting of a three-dimensional beam: Deformation of the SBM formulation with enclosed surrogate boundary ($\tilde{\Omega}_0^h \subset \Omega_0$). Fig. 11(a) displays the surrogate boundary deformation (blue) and the true boundary deformation reconstructed with (37) (transparent gray), for an SBM simulation with 1731 active elements. In Fig. 11(b), the deformation of a body-fitted simulation (blue) with a mesh consisting of 1940 elements is superimposed on that of the SBM-reconstructed true boundary (gray). Fig. 11(c) is a zoomed view of Fig. 11(b). Fig. 11(d) displays the surrogate boundary deformation (blue) and the reconstructed true boundary deformation (transparent gray), for an SBM simulation with 140,617 active elements. In Fig. 11(e), the deformation of a body-fitted simulation (blue) with a mesh consisting of 135,831 elements is superimposed on that of the SBM-reconstructed true boundary (gray). Fig. 11(f) is a zoomed view of Fig. 11(e). (For interpretation of the references to color in this figure legend, the reader is referred to the web version of this article.)

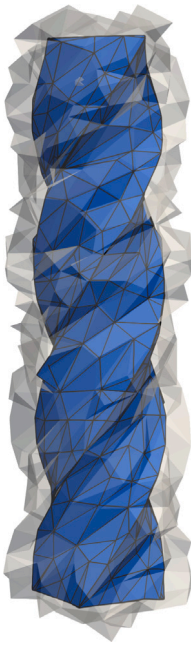

(a) Coarse grid: the surrogate boundary (gray) and the SBM-reconstructed true boundary (blue).

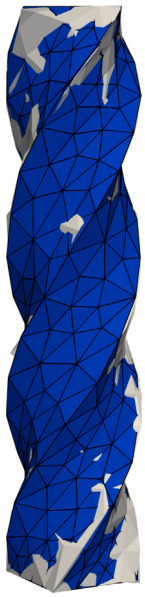

(b) Course grid: the boundary of a body-fitted computation (blue) and the SBM-reconstructed true boundary (gray).

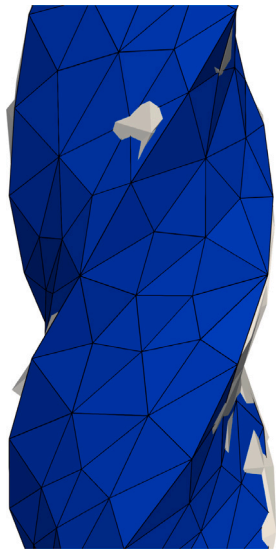

(c) Zoomed view of Figure 12b.

(d) Fine grid: the surrogate boundary (gray) and the SBM-reconstructed true boundary (blue).

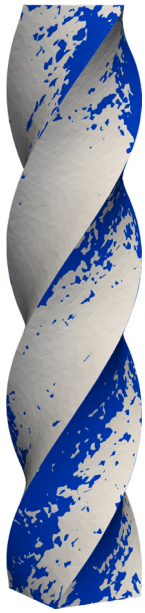

(e) Fine grid: the boundary of a body-fitted computation (blue) and the SBM-reconstructed true boundary (gray).

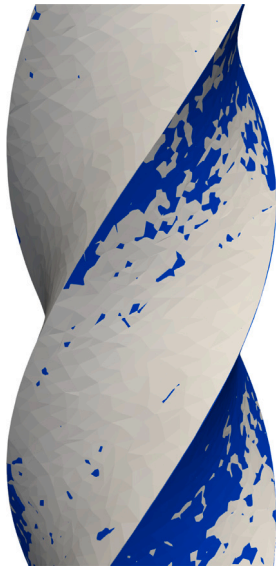

(f) Zoomed view of Figure 12e.

Fig. 12. Twisting of a three-dimensional beam: Deformation of the SBM formulation with enclosing surrogate boundary ($\Omega_0 \subset \tilde{\Omega}_0^h$). Fig. 12(a) displays the surrogate boundary deformation (transparent gray) and the true boundary deformation reconstructed with (37) (blue), for an SBM simulation with 2040 active elements. In Fig. 12(b), the deformation of a body-fitted simulation (blue) with a mesh consisting of 1940 elements is superimposed on that of the SBM-reconstructed true boundary (gray). Fig. 12(c) is a zoomed view of Fig. 12(b). Fig. 12(d) displays the surrogate boundary deformation (transparent gray) and the reconstructed true boundary (blue), for an SBM simulation with 143,854 active elements. In Fig. 12(e), the deformation of a body-fitted simulation (blue) with a mesh consisting of 135,831 elements is superimposed on that of the SBM-reconstructed true boundary (gray). Fig. 12(f) is a zoomed view of Fig. 12(e). (For interpretation of the references to color in this figure legend, the reader is referred to the web version of this article.)

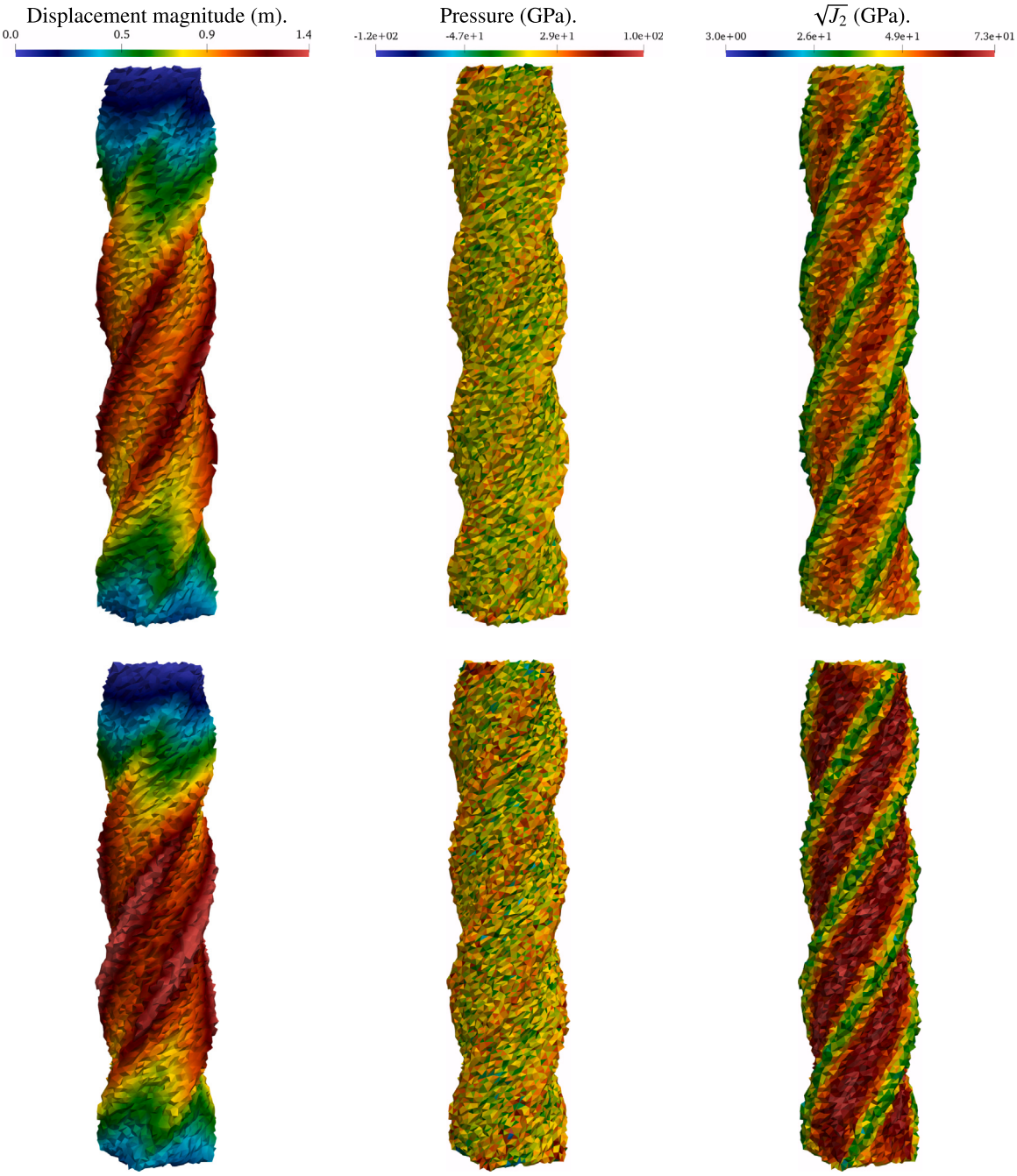

Fig. 13. Twisting of a three-dimensional beam on the finest grids: contour plots of the displacement magnitude, the volumetric stress (pressure), and the square root of the von Mises stress ($\sqrt{J_2}$). The first row refers to the enclosed surrogate case ($\tilde{\Omega}_0^h \subset \Omega_0$) and the second row to the enclosing surrogate case ($\Omega_0 \subset \tilde{\Omega}_0^h$). Color contours are shown on the surrogate boundary. (For interpretation of the references to color in this figure legend, the reader is referred to the web version of this article.)

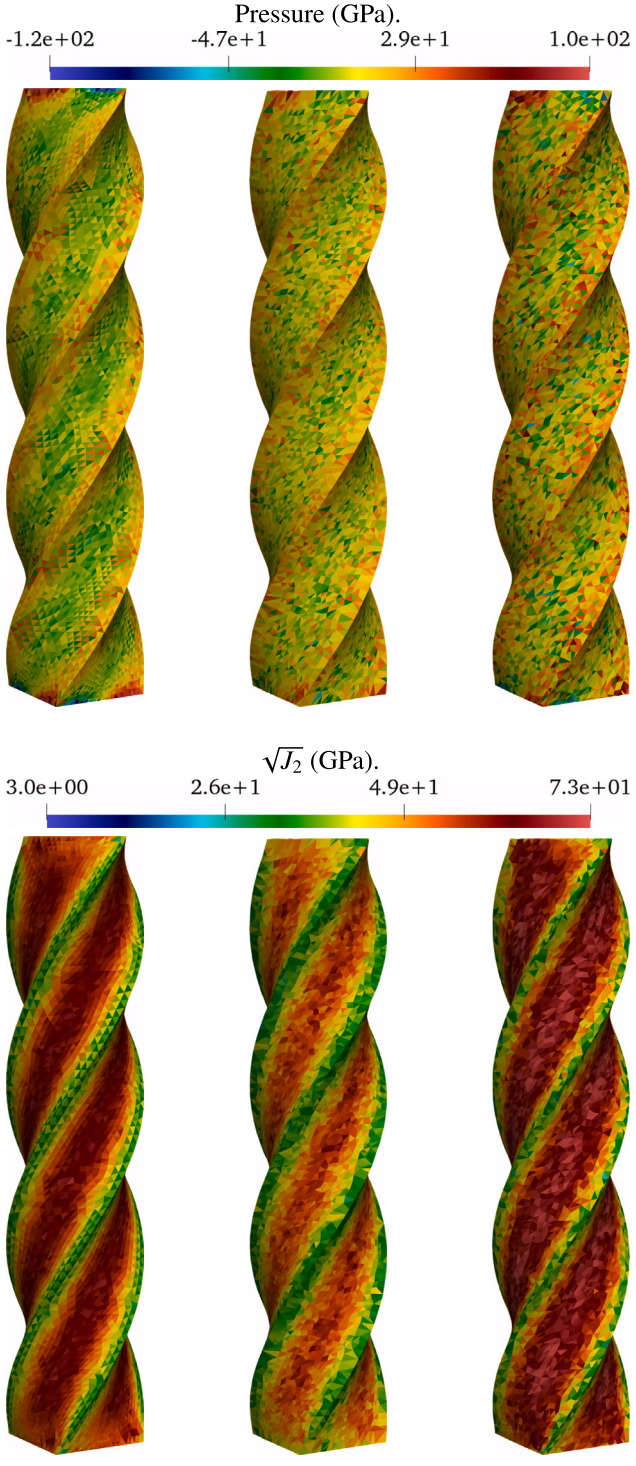

Fig. 14. Twisting of a three-dimensional beam: contour plots of the volumetric stress (pressure) and the square root of the von Mises stress ($\sqrt{J_2}$). Color contours are shown on the true boundary geometry, reconstructed with (37). Similarly, stresses for the SBM are post-processed on the true boundary using the strategy described in Section 4.1. The first column refers to the body-fitted simulation, the second column to the enclosed surrogate case ($\tilde{\Omega}_0^h \subset \Omega_0$) and the third column to the enclosing surrogate case ($\Omega_0 \subset \tilde{\Omega}_0^h$). (For interpretation of the references to color in this figure legend, the reader is referred to the web version of this article.)

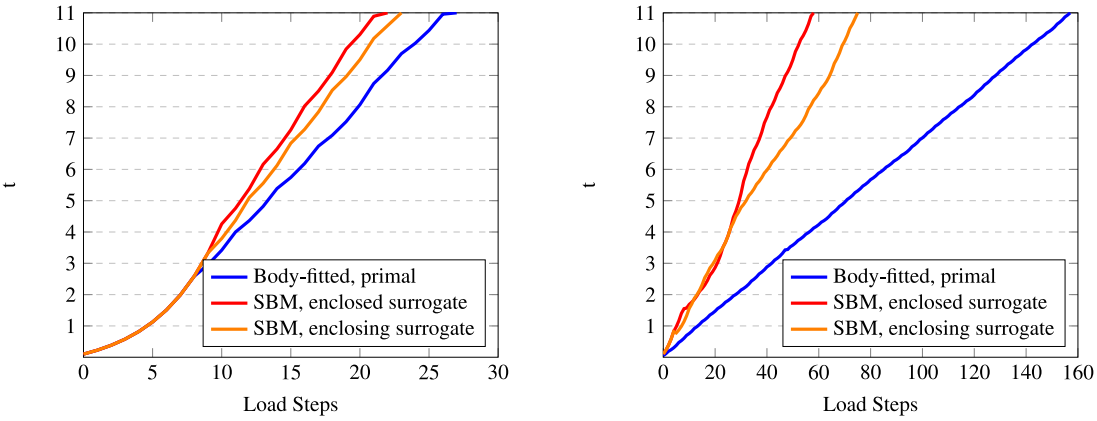

Fig. 15. Twisting of a three-dimensional beam: history of the loading parameter t, for both coarse grids (left) and fine grids (right).

Table 2
Bending of a three-dimensional beam: Initial load step and number of load steps for SBM and body-fitted formulations.

Formulation	No. elements	No. active elements	Initial load step	No. loading steps
SBM ($\tilde{\Omega}_0^h \subset \Omega_0$)	25,150 1,105,763	1731 140,617	0.1 0.025	31 171
SBM ($\Omega_0 \subset \tilde{\Omega}_0^h$)	5658 641,390	2040 143,854	0.05 0.01	72 244
Body-fitted	1940 135,831	1940 135,831	0.05 0.0125	84 409

the body-fitted simulations. Possibly, the SBM with enclosing surrogate offers slightly more accurate solution than the SBM with enclosed surrogate.

Finally, Table 1 reports the initial load step and the number of loading steps for the SBM and body-fitted calculations and Fig. 15 shows the load step history in reaching the final load. It is clear that the SBM calculations require fewer load steps to reach the final load. This is result is in part due to the fact that the SBM adopts the weak imposition of the boundary conditions, which results in more robust Newton iteration cycles.

4.5. Bending a three-dimensional beam

Next we consider a bending problem for a structure with the same beam-like geometry, material parameters, and computational grids used in the previous twist test. Also the boundary conditions are the same, except for the Dirichlet conditions on the top boundary, which are now given by

$$\boldsymbol{u} = \begin{Bmatrix} u_x \\ u_y \\ u_z \end{Bmatrix} = \begin{Bmatrix} x\cos(t\,\pi/6) - y\sin(t\,\pi/6) - x \\ x\sin(t\,\pi/6) + y\cos(t\,\pi/6) - y \\ 0 \end{Bmatrix} \text{ m} , \tag{39}$$

with a loading parameter t that is progressively increased from 0 to 5.

We adopt the same adaptive loading strategy described in the twisting beam test described in Section 4.4.

We present the results in a form analogous to the previous twisting-beam test. In particular, Figs. 16, 17, 18, and 19 correspond, for this test, to Figs. 11, 12, 13, and 14 for the previous test. The conclusions that we can draw are very similar. On fine grids, the SBM results are very similar to the results of body-fitted primal computations.

The bending test described here is more demanding, in term of robustness, than the twisting beam problem described in the previous section, since it produces more severe states of deformation. The reason lies on the fact that the stress and deformation patterns due to bending are much more complex than in the case of twisting and this is reflected in the increased number of load steps to reach the final stage of deformation. Table 2 records the initial load step and the number of loading steps for the SBM and body-fitted calculations and Fig. 20 shows the load step history in reaching the final load. Also in this case it is evident that the SBM calculations require fewer number of load steps to reach the final load state. Like in the previous case of twisting deformation, the SBM with enclosed surrogate appears more efficient than the SBM with enclosing surrogate.

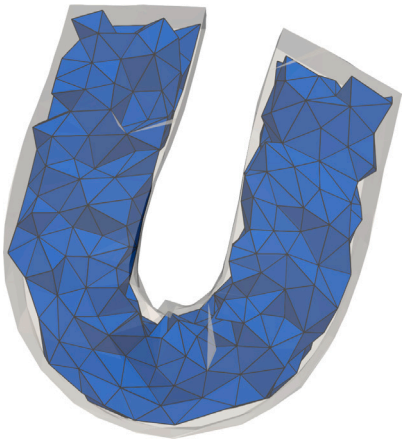

(a) Coarse grid: the surrogate boundary (blue) and the SBM-reconstructed true boundary (gray).

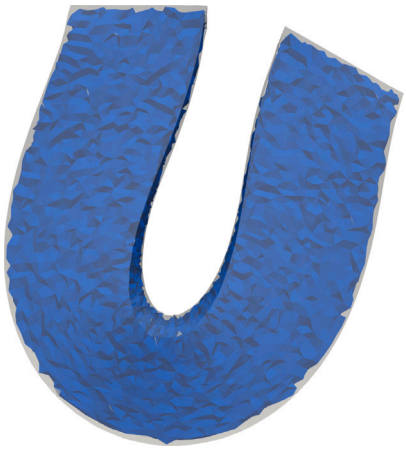

(b) Fine grid: the surrogate boundary (blue) and the SBM-reconstructed true boundary (gray).

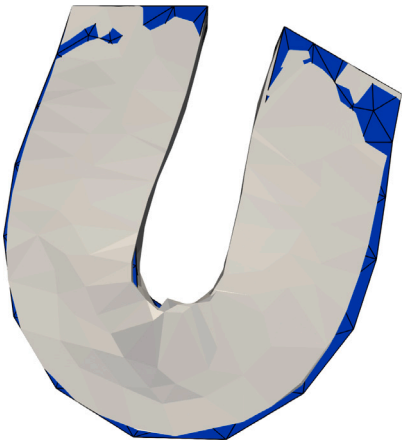

(c) Coarse grid: the boundary of a body-fitted computation (blue) and the SBM-reconstructed true boundary (gray).

(d) Fine grid: the boundary of a body-fitted computation (blue) and the SBM-reconstructed true boundary (gray).

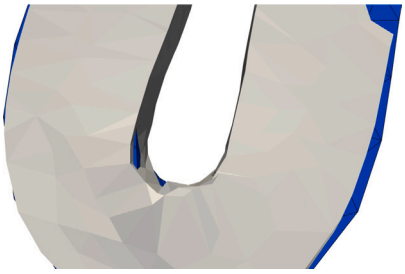

(e) Zoomed view of Figure 16c.

(f) Zoomed view of Figure 16d.

Fig. 16. Bending of a three-dimensional beam: Deformation of the SBM formulation with enclosed surrogate boundary ($\tilde{\Omega}_0^h \subset \Omega_0$). Fig. 16(a) displays the surrogate boundary deformation (blue) and the true boundary deformation reconstructed with (37) (transparent gray), for an SBM simulation with 1731 active elements. In Fig. 16(c), the deformation of a body-fitted simulation (blue) with a mesh consisting of 1940 elements is superimposed on that of the SBM-reconstructed true boundary (gray). Fig. 16(e) is a zoomed view of Fig. 16(c). Fig. 16(b) displays the surrogate boundary deformation (blue) and the reconstructed true boundary deformation (transparent gray), for an SBM simulation with 140,617 active elements. In Fig. 16(d), the deformation of a body-fitted simulation (blue) with a mesh consisting of 135,831 elements is superimposed on that of the SBM-reconstructed true boundary (gray). Fig. 16(f) is a zoomed view of Fig. 16(d). (For interpretation of the references to color in this figure legend, the reader is referred to the web version of this article.)

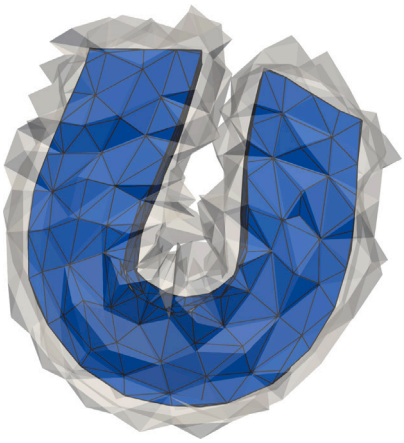

(a) Coarse grid: the surrogate boundary (gray) and the SBM-reconstructed true boundary (blue).

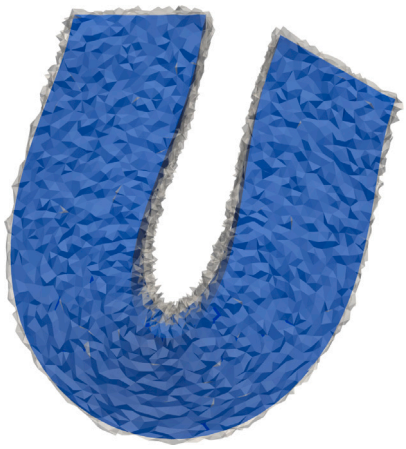

(b) Fine grid: the surrogate boundary (gray) and the SBM-reconstructed true boundary (blue).

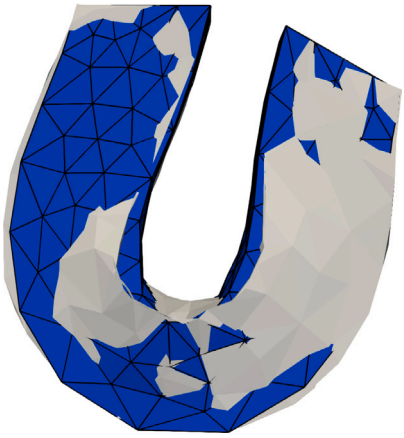

(c) Coarse grid: the boundary of a body-fitted computation (blue) and the SBM-reconstructed true boundary (gray).

(d) Fine grid: the boundary of a body-fitted computation (blue) and the SBM-reconstructed true boundary (gray).

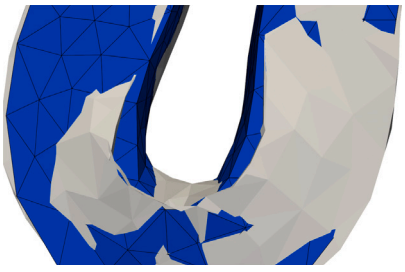

(e) Zoomed view of Figure 16c.

(f) Zoomed view of Figure 16d.

Fig. 17. Bending of a three-dimensional beam: Deformation of the SBM formulation with enclosing surrogate boundary ($\Omega_0 \subset \tilde{\Omega}_0^h$). Fig. 17(a) displays the surrogate boundary deformation (transparent gray) and the true boundary deformation reconstructed with (37) (blue), for an SBM simulation with 2040 active elements. In Fig. 17(c), the deformation of a body-fitted simulation (blue) with a mesh consisting of 1940 elements is superimposed on that of the SBM-reconstructed true boundary (gray). Fig. 17(e) is a zoomed view of Fig. 17(c). Fig. 17(b) displays the surrogate boundary deformation (transparent gray) and the reconstructed true boundary (blue), for an SBM simulation with 143,854 active elements. In Fig. 17(d), the deformation of a body-fitted simulation (blue) with a mesh consisting of 135,831 elements is superimposed on that of the SBM-reconstructed true boundary (gray). Fig. 17(f) is a zoomed view of Fig. 17(d). (For interpretation of the references to color in this figure legend, the reader is referred to the web version of this article.)

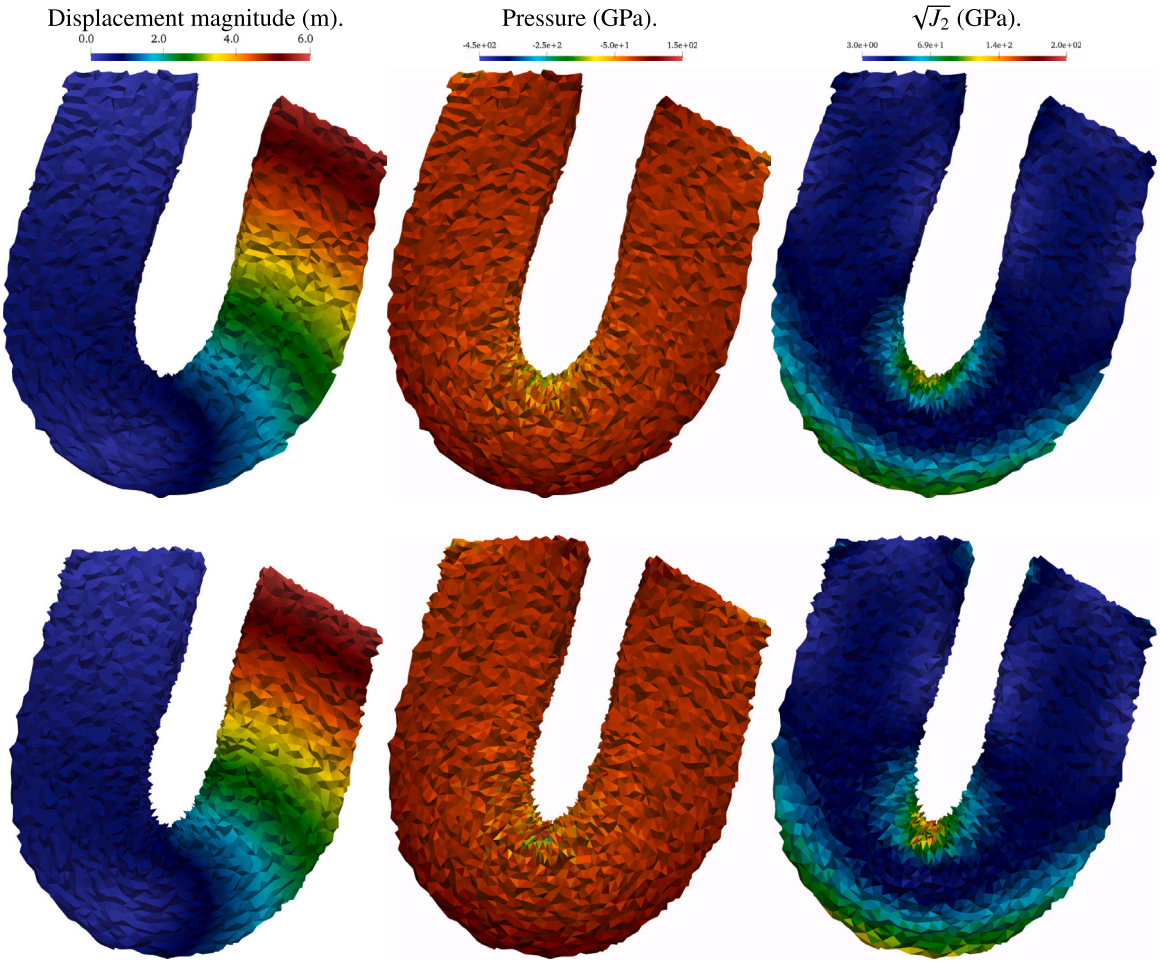

Fig. 18. Bending of a three-dimensional beam computed with the SBM on the finest grids: contour plots of the displacement magnitude, the volumetric stress (pressure), and the square root of the von Mises stress ($\sqrt{J_2}$). The first row refers to the enclosed surrogate case ($\tilde{\Omega}_0^h \subset \Omega_0$) and the second row to the enclosing surrogate case ($\Omega_0 \subset \tilde{\Omega}_0^h$).

4.6. *Bending a three-dimensional beam with nominal Poisson ratio* $\nu = 0.30$

Next we consider again same bending test in Section 4.5 with the same geometry, boundary conditions, loading conditions, and adaptive loading strategy. However, we set a bulk modulus $\kappa = 208.33$ and a shear modulus $\mu = 96.15$ such that the nominal Poisson ratio is 0.30.

Under this setup, the body-fitted calculation on the finest grid was only able to reach $t = 4.95372$ while the SBM numerical calculations for both the enclosed surrogate domain ($\tilde{\Omega}_0^h \subset \Omega_0$) and the enclosing surrogate domain ($\tilde{\Omega}_0^h \subset \Omega_0$) successfully reached $t = 5$ on the finest grids.

Given the more compressible nature of the material with respect to the previous case of a nominal Poisson ratio of 0.45, the overall mechanical system is less stiff and there is a higher possibility for elements from either sides of the beam to interpenetrate each other at a certain point (we do not implement a contact algorithm in this test). The body-fitted calculation breaks down just before this occurs while the SBM calculations continue until the end, despite elements interpenetrate, as shown in Fig. 21.

Fig. 22 shows contours of the SBM displacement, post-processed pressure and square root of the von Mises stress ($\sqrt{J_2}$) on the finest grids, for both the enclosed surrogate domain ($\tilde{\Omega}_0^h \subset \Omega_0$) and the enclosing surrogate domain ($\tilde{\Omega}_0^h \subset \Omega_0$).

The displacement field is stable, smooth and free from spurious oscillations, however we start observing severe stress concentrations of the pressure and square root of the von Mises stress ($\sqrt{J_2}$) fields in certain elements of the mesh. This is an indication that more refined grids are required to fully resolve the stress fields, but this aspect is beyond the scope of the present paper, considering the size of the computations. We can however conclude that the SBM is at least as robust as a body-fitted primal finite element, if not more robust.

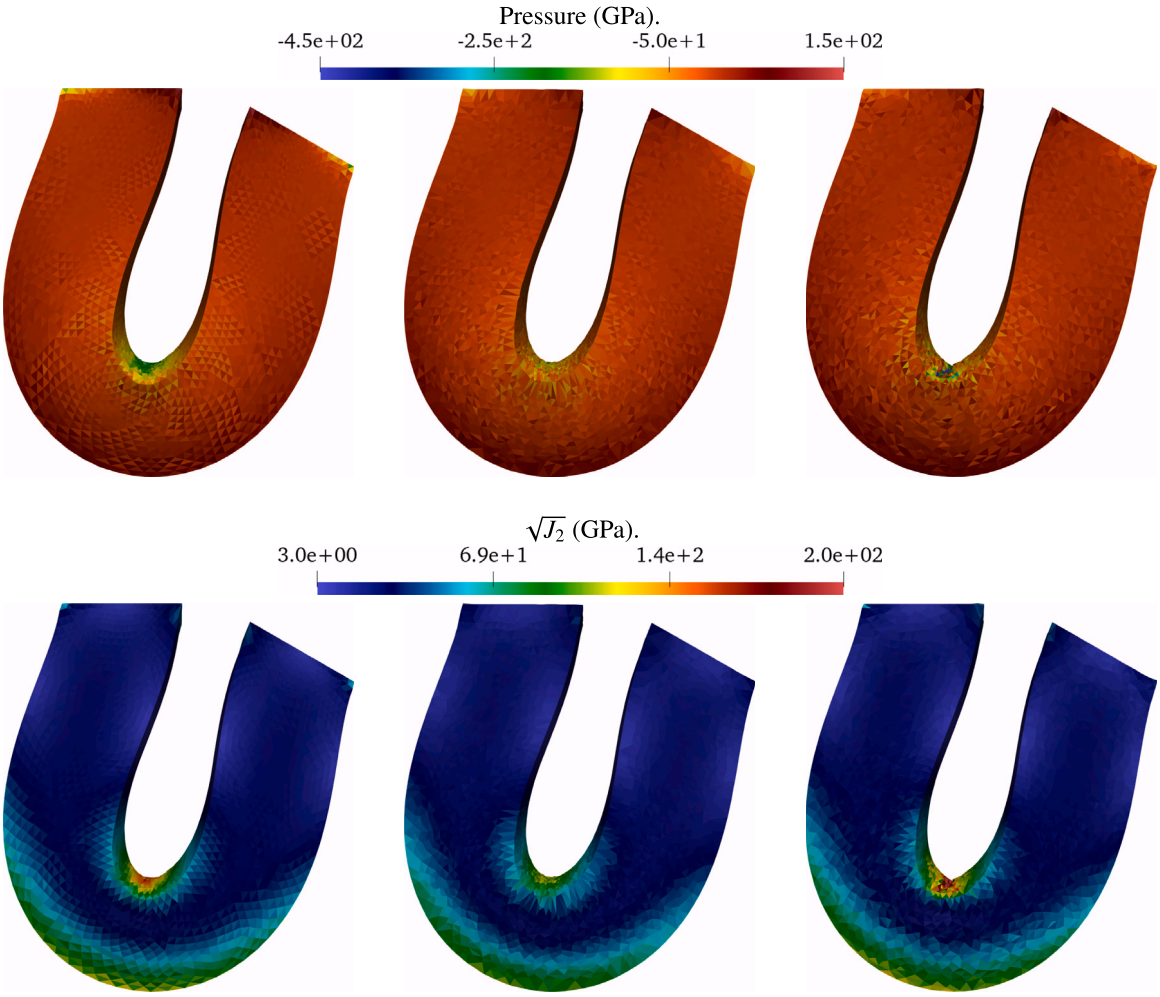

Fig. 19. Bending of a three-dimensional beam: contour plots of the volumetric stress (pressure) and the square root of the von Mises stress ($\sqrt{J_2}$) on the body-fitted and reconstructed true deformed shape. Color contours are shown on the true boundary geometry, reconstructed with (37). Similarly, stresses for the SBM are post-processed on the true boundary using the strategy described in Section 4.1. The first column refers to the body-fitted simulation, the second column to the SBM with enclosed surrogate ($\bar{\Omega}_0^h \subset \Omega_0$) and the third column to the SBM with enclosing surrogate ($\Omega_0 \subset \bar{\Omega}_0^h$). (For interpretation of the references to color in this figure legend, the reader is referred to the web version of this article.)

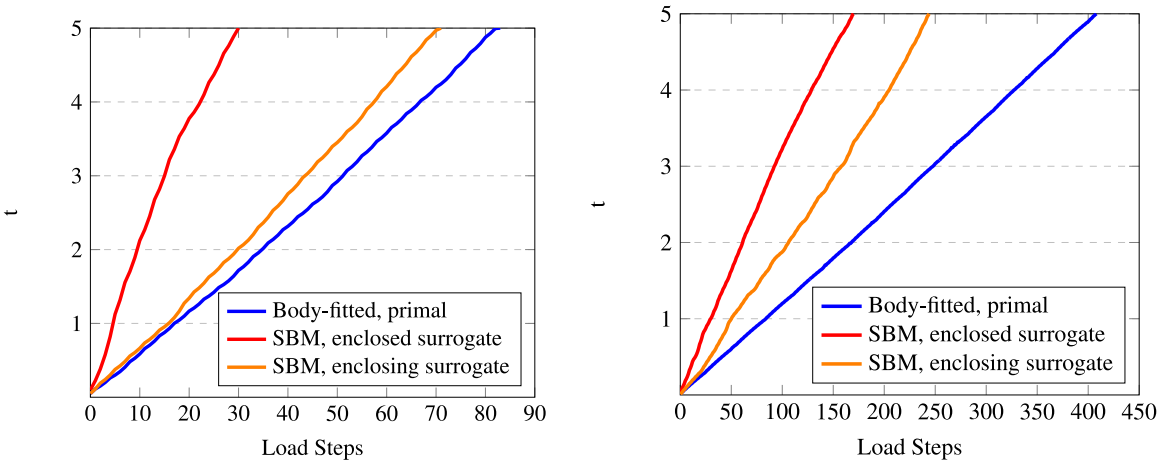

Fig. 20. Bending of a three-dimensional beam: history of the loading parameter t as the load steps increase, for both coarse grids (left) and fine grids (right).

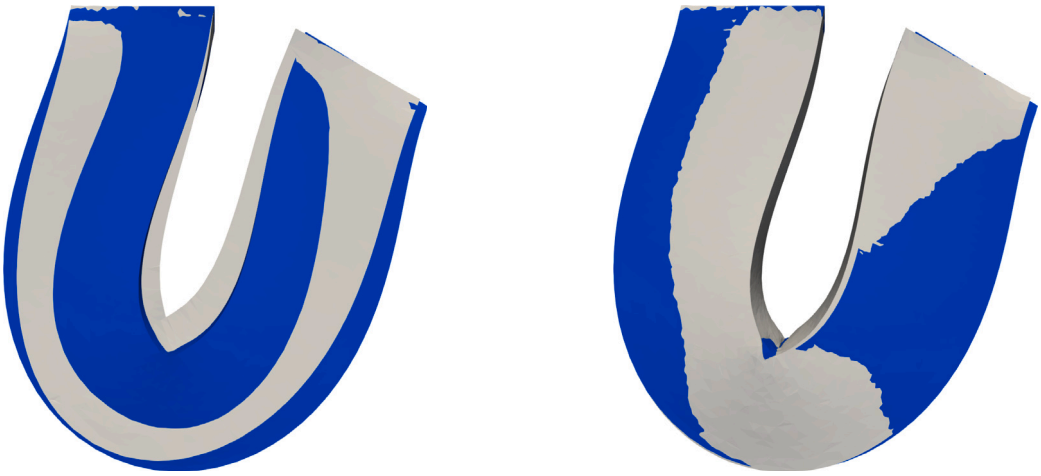

(a) Enclosed surrogate domain: the body-fitted (blue) and SBM-reconstructed (gray) surfaces.

(b) Enclosing surrogate domain: the body-fitted (blue) and SBM-reconstructed (gray) surfaces.

Fig. 21. Bending of a three-dimensional beam on the finest grids for a nominal Poisson ratio $\nu = 0.30$: Deformation of the SBM formulation with the enclosed surrogate domain (Fig. 21(a)) and enclosing surrogate domain (Fig. 21(b)) superimposed against the body-fitted simulation. Deformation is reconstructed according to (37). (For interpretation of the references to color in this figure legend, the reader is referred to the web version of this article.)

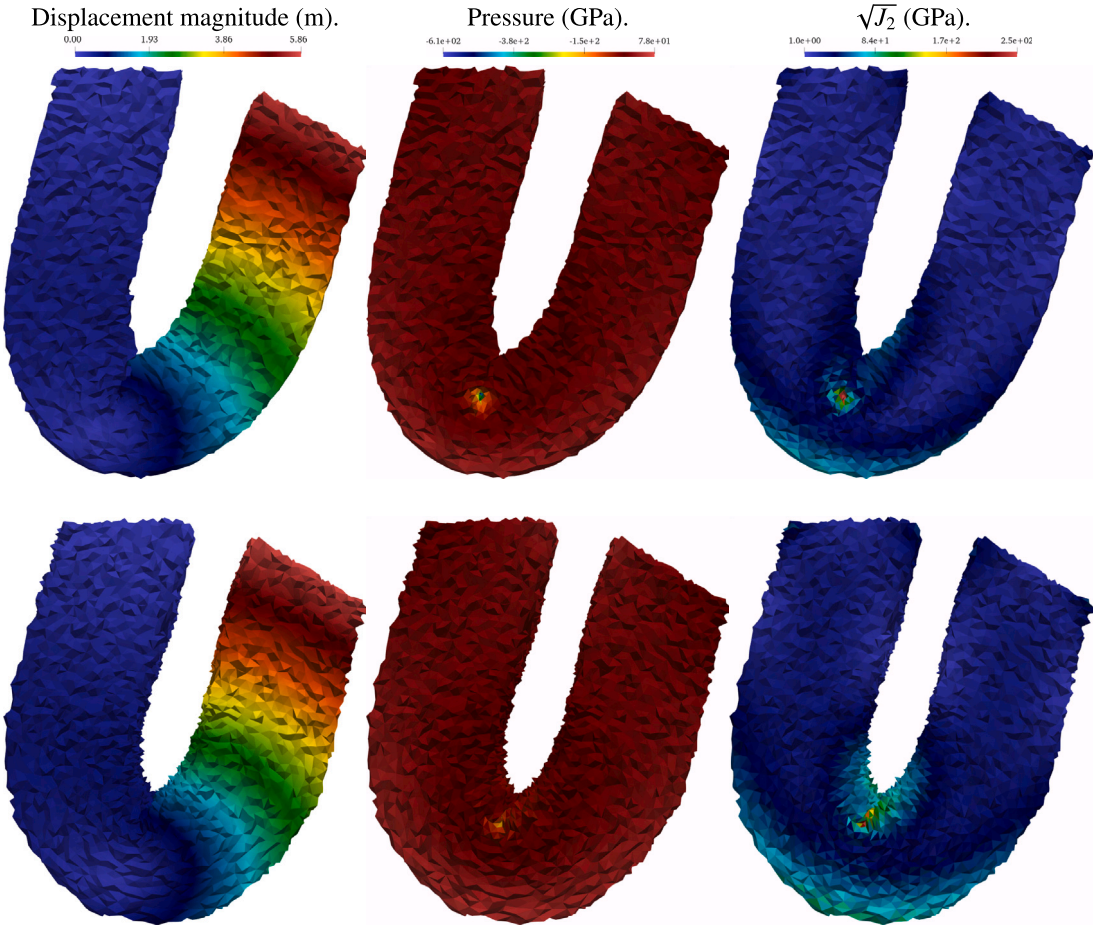

Fig. 22. Bending of a three-dimensional beam computed with the SBM on the finest grids for a nominal Poisson ratio $\nu = 0.30$: Contours of the displacement magnitude, the volumetric stress (pressure) and the square root of the von Mises stress ($\sqrt{J_2}$). The first row refers to the enclosed surrogate case ($\tilde{\Omega}_0^h \subset \Omega_0$), and the second row to the enclosing surrogate case ($\Omega_0 \subset \tilde{\Omega}_0^h$).

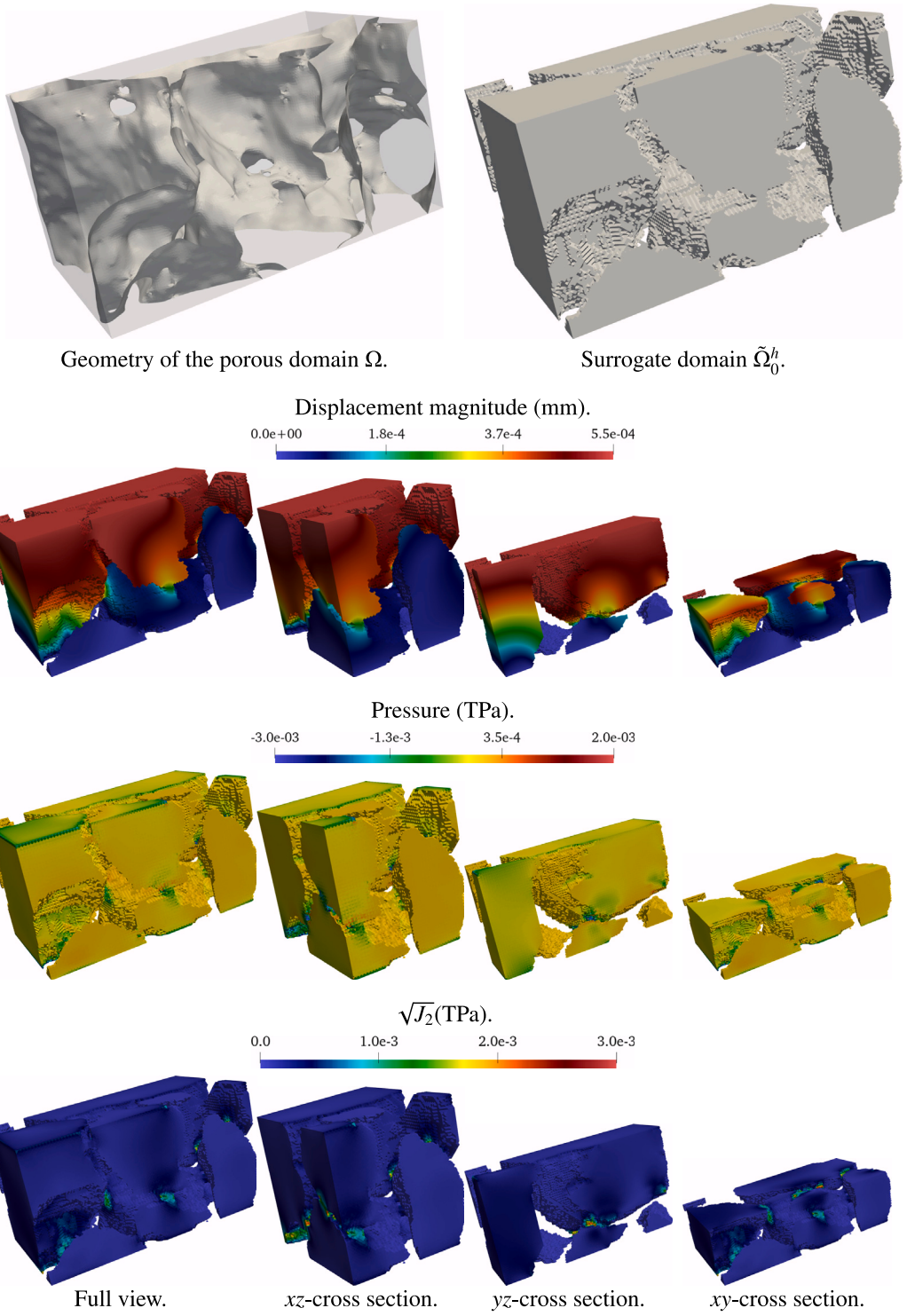

Fig. 23. Compression of a porous specimen. The geometry of the true domain Ω_0, the surrogate domain $\tilde{\Omega}_0^h$, and contours of the displacement magnitude, the volumetric (pressure) stress, and the square root of the von Mises stress ($\sqrt{J_2}$), for various cross-sections (mid-planes), on the deformed configuration.

Table 3
Setup times for the test involving the compression of a porous specimen.

No. elements	No. active elements	No. cores	No. true surface facets	Setup time (s)
5,229,000	3,458,639	240	112,629	217

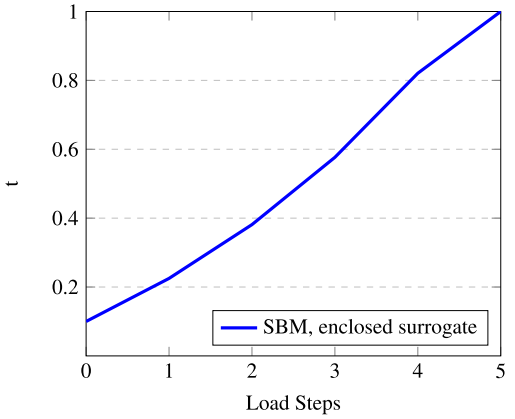

Fig. 24. Compression of a porous specimen: Plot of t as the load steps are increased.

4.6.1. Compression of a porous specimen

Finally, we consider a domain with a geometry that has been obtained via imaging techniques [61]. As shown at the top left of Fig. 23, we consider a sample of a porous material, that is the domain $\Omega_0 = [0, 0.3]\ \text{mm} \times [0, 0.5]\ \text{mm} \times [0.2, 0.47]\ \text{mm}$, that has been subdivided in voxels of size $8.33 \cdot\ \mu\text{m} \times 8.33 \cdot\ \mu\text{m} \times 8.33 \cdot\ \mu\text{m}$, by CT-scan techniques. The voxel representation of the sample has then been segmented in STL format (i.e., a set of disconnected triangular facets, which do not necessarily combine to form a water-tight surface), to represent the interface between the material and the voids.

The displacement on the top side surface is set to $\boldsymbol{u} = \{0.0\ \text{mm}, -0.54t\ \text{mm}, 0.0\ \text{mm}\}^T$, where t is increased from 0 to 1. The solid is clamped ($\boldsymbol{u} = \boldsymbol{0}$) at the bottom surface and traction-free boundary conditions are imposed elsewhere. Given the geometric setup of the problem, we set $\bar{l}(\Omega_0) = 0.5\ \text{mm}$ while the material parameters and loading strategy are the same as for the beam twisting test presented in Section 4.4, with an initial load step of 0.1.

As apparent, the geometric features of this problem include a large number of fissures, holes and cracks which make body-fitted meshing very challenging, particularly since the (computational) interface rock/void is not watertight. It is in this situations that the power of an immersed/embedded solid mechanics method becomes clear, since the intersection of the interface solid/void with the background grid is an operation that is inherently parallelizable and much more robust and efficient than body-fitted mesh generation. We point out that this initial geometry cleanup phase is completely automated and parallelized, as opposed to the typical geometry cleanup in body-fitted grids and/or CAD models, which requires the direct intervention of the user.

Table 3 shows the SBM setup time to be less than 4 minutes. The setup time includes the time it takes to: (a) compute intersections between the STL surface that defines the boundary and the background grid; (b) generate the surrogate domain and boundaries; and (c) calculate the distance vector along the surrogate boundary. To have a reference, the SBM setup time must be compared with the time it takes, in a body-fitted computation, to convert STL to CAD format, including geometry cleanup operations, and the time it takes to mesh the geometry. We can expect the setup phase for the SBM to be smaller, by one to two orders of magnitude, than the typical setup times required by CAD and body-fitted grid generation tools.

Numerical results are computed using the SBM with enclosed surrogate domain shown at the top right of Fig. 23. A total of 6 loading steps were needed to reach the final load state, as shown in the load step history presented in Fig. 24. The three bottom rows of Fig. 23 display the displacement magnitude, volumetric stress, and square root of the von Mises stress ($\sqrt{J_2}$), respectively. Much like in the previous three-dimensional tests, the numerical solution is smooth and well-behaved, indicating that the SBM can serve as a valuable tool in the emerging imaging-to-computing field or for the training of geometrically parametrized Digital Twins.

5. Conclusions

We presented a Shifted Boundary Method for nonlinear mechanics, in the class of immersed solid mechanic methods, which proved robust in a series of classical benchmark tests and effective in simulating very complex geometries.

Because no cut-cells are present in the formulation, standard Gauss quadrature formulas can be used, and this is a major advantage with respect to other immersed methods, which typically require orders of magnitude more quadrature points than standard finite elements, to integrate the governing equations over cut cells.

This in turn results in an algorithm with computational cost very similar to traditional body-fitted finite element methods, but without the mesh generation overhead associated with simulations in complex geometry.

Future work will be directed to attack nonlinear incompressible elasticity and inelasticity, which however are not foreseen to be problematic, since the SBM can be adapted easily to formulations encompassing such problems. The simulation of nonlinear buckling with the SBM is also expected to be feasible, although beyond the scope of the present work.

CRediT authorship contribution statement

Nabil M. Atallah: Conceptualization, Investigation, Methodology, Software, Validation, Writing – original draft, Writing – review & editing. **Guglielmo Scovazzi:** Conceptualization, Investigation, Methodology, Supervision, Writing – original draft, Writing – review & editing.

Declaration of competing interest

The authors declare that they have no known competing financial interests or personal relationships that could have appeared to influence the work reported in this paper.

Data availability

Data will be made available on request.

Acknowledgments

This work was performed under the auspices of the U.S. Department of Energy by Lawrence Livermore National Laboratory under Contract DE-AC52-07NA27344 and the LLNL-LDRD Program under Grant 21-ERD-031 (LLNL-JRNL-854800). Guglielmo Scovazzi gratefully acknowledges the support of the LLNL-LDRD Program under Grant 21-ERD-031 (LLNL-JRNL-854800) and the support of the National Science Foundation, Division of Mathematical Sciences (DMS), under Grant 2207164.

References

[1] Jamshid Parvizian, Alexander Düster, Ernst Rank, Finite cell method, Comput. Mech. 41 (1) (2007) 121–133.
[2] Alexander Düster, Jamshid Parvizian, Zhengxiong Yang, Ernst Rank, The finite cell method for three-dimensional problems of solid mechanics, Comput. Methods Appl. Mech. Engrg. 197 (45) (2008) 3768–3782.
[3] Peter Hansbo, Mats G. Larson, Karl Larsson, Cut finite element methods for linear elasticity problems, in: Geometrically Unfitted Finite Element Methods and Applications, Springer, 2017, pp. 25–63.
[4] Jamshid Parvizian, Aexander Düster, Ernst Rank, Topology optimization using the finite cell method, Opt. Eng. 13 (1) (2012) 57–78.
[5] Kosala Bandara, Thomas Rüberg, Fehmi Cirak, Shape optimisation with multiresolution subdivision surfaces and immersed finite elements, Comput. Methods Appl. Mech. Engrg. 300 (2016) 510–539.
[6] Erik Burman, Daniel Elfverson, Peter Hansbo, Mats G Larson, Karl Larsson, Shape optimization using the cut finite element method, Comput. Methods Appl. Mech. Engrg. 328 (2018) 242–261.
[7] J. Nitsche, Uber ein Variationsprinzip zur Losung Dirichlet-Problemen bei Verwendung von Teilraumen, die keinen Randbedingungen unteworfen sind, Abh. Math. Semin. Univ. Hambg. 36 (1) (1971) 9–15.
[8] Anita Hansbo, Peter Hansbo, An unfitted finite element method, based on Nitsche's method, for elliptic interface problems, Comput. Methods Appl. Mech. Engrg. 191 (47) (2002) 5537–5552.
[9] Nicolas Moës, John Dolbow, Ted Belytschko, A finite element method for crack growth without remeshing, Int. J. Numer. Methods Eng. 46 (1) (1999) 131–150.
[10] Alex Main, Guglielmo Scovazzi, The shifted boundary method for embedded domain computations. Part I: Poisson and Stokes problems, J. Comput. Phys. 372 (2018) 972–995.
[11] Alex Main, Guglielmo Scovazzi, The shifted boundary method for embedded domain computations. Part II: Linear advection–diffusion and incompressible Navier-Stokes equations, J. Comput. Phys. 372 (2018) 996–1026.
[12] Ting Song, Alex Main, Guglielmo Scovazzi, Mario Ricchiuto, The shifted boundary method for hyperbolic systems: Embedded domain computations of linear waves and shallow water flows, J. Comput. Phys. 369 (2018) 45–79.
[13] Oriol Colomés, Alex Main, Léo Nouveau, Guglielmo Scovazzi, A weighted Shifted Boundary Method for free surface flow problems, J. Comput. Phys. 424 (2021) 109837.
[14] Nabil M. Atallah, Claudio Canuto, Guglielmo Scovazzi, Analysis of the shifted boundary method for the Stokes problem, Comput. Methods Appl. Mech. Engrg. 358 (2020) 112609.
[15] J Austin Cottrell, Alessandro Reali, Yuri Bazilevs, Thomas JR Hughes, Isogeometric analysis of structural vibrations, Comput. Methods Appl. Mech. Engrg. 195 (41) (2006) 5257–5296.
[16] Yuri Bazilevs, Victor M Calo, John A Cottrell, John A Evans, Thomas Jr R Hughes, S Lipton, Michael A Scott, Thomas W Sederberg, Isogeometric analysis using T-splines, Comput. Methods Appl. Mech. Engrg. 199 (5) (2010) 229–263.
[17] Dominik Schillinger, Luca Dede, Michael A Scott, John A Evans, Michael J Borden, Ernst Rank, Thomas JR Hughes, An isogeometric design-through-analysis methodology based on adaptive hierarchical refinement of NURBS, immersed boundary methods, and T-spline CAD surfaces, Comput. Methods Appl. Mech. Engrg. 249–252 (2012) 116–150.
[18] Annalisa Buffa, Ondine Chanon, Rafael Vázquez, An a posteriori error estimator for isogeometric analysis on trimmed geometries, IMA J. Numer. Anal. 43 (5) (2023) 2533–2561.
[19] Xiaodong Wei, Riccardo Puppi, Pablo Antolin, Annalisa Buffa, Stabilized isogeometric formulation of the Stokes problem on overlapping patches, Comput. Methods Appl. Mech. Engrg. 417 (2023) 116477, http://dx.doi.org/10.1016/j.cma.2023.116477.
[20] Pablo Antolin, Xiaodong Wei, Annalisa Buffa, Robust numerical integration on curved polyhedra based on folded decompositions, Comput. Methods Appl. Mech. Engrg. 395 (2022) 114948.
[21] Luca Coradello, Pablo Antolin, Rafael Vázquez, Annalisa Buffa, Adaptive isogeometric analysis on two-dimensional trimmed domains based on a hierarchical approach, Comput. Methods Appl. Mech. Engrg. 364 (2020) 112925.

[22] Jochen Hinz, Annalisa Buffa, PDE-based parameterisation techniques for planar multipatch domains, 2023, arXiv preprint arXiv:2307.06265.
[23] Annalisa Buffa, Ondine Chanon, Rafael Vázquez, Analysis-aware defeaturing: problem setting and a posteriori estimation, Math. Models Methods Appl. Sci. 32 (02) (2022) 359–402.
[24] Pablo Antolin, Annalisa Buffa, Riccardo Puppi, Xiaodong Wei, Overlapping multipatch isogeometric method with minimal stabilization, SIAM J. Sci. Comput. 43 (1) (2021) A330–A354.
[25] Leo Nouveau, Mario Ricchiuto, Guglielmo Scovazzi, High-order gradients with the shifted boundary method: An embedded enriched mixed formulation for elliptic PDEs, J. Comput. Phys. 398 (2019) 108898.
[26] Erik Burman, Ghost penalty, C. R. Math. 348 (21) (2010) 1217–1220.
[27] Erik Burman, Peter Hansbo, Fictitious domain methods using cut elements: III. A stabilized Nitsche method for Stokes' problem, ESAIM Math. Model. Numer. Anal. 48 (3) (2014) 859–874.
[28] B. Schott, U. Rasthofer, V. Gravemeier, W.A. Wall, A face-oriented stabilized Nitsche-type extended variational multiscale method for incompressible two-phase flow, Internat. J. Numer. Methods Engrg. 104 (7) (2015) 721–748.
[29] B. Schott, W.A. Wall, A new face-oriented stabilized XFEM approach for 2D and 3D incompressible Navier–Stokes equations, Comput. Methods Appl. Mech. Engrg. 276 (2014) 233–265.
[30] Nabil M. Atallah, Claudio Canuto, Guglielmo Scovazzi, The high-order shifted boundary method and its analysis, Comput. Methods Appl. Mech. Engrg. 394 (2022) 114885.
[31] J. Haydel Collins, Alexei Lozinski, Guglielmo Scovazzi, A penalty-free shifted boundary method of arbitrary order, Comput. Methods Appl. Mech. Engrg. 417 (2023) 116301, A Special Issue in Honor of the Lifetime Achievements of T. J. R. Hughes.
[32] Nabil M. Atallah, Claudio Canuto, Guglielmo Scovazzi, The Shifted Boundary Method for solid mechanics, Internat. J. Numer. Methods Engrg. 122 (20) (2021) 5935–5970.
[33] Kangan Li, Nabil M Atallah, G Alex Main, Guglielmo Scovazzi, The Shifted Interface Method: a flexible approach to embedded interface computations, Internat. J. Numer. Methods Engrg. 121 (3) (2020) 492–518.
[34] Kangan Li, Nabil M Atallah, Antonio Rodríguez-Ferran, Dakshina M Valiveti, Guglielmo Scovazzi, The Shifted Fracture Method, Internat. J. Numer. Methods Engrg. 122 (22) (2021) 6641–6679.
[35] Kangan Li, Antonio Rodríguez-Ferran, Guglielmo Scovazzi, A blended Shifted-Fracture/Phase-Field framework for sharp/diffuse crack modeling, Internat. J. Numer. Methods Engrg. 124 (4) (2023) 998–1030.
[36] Kangan Li, Antonio Rodríguez-Ferran, Guglielmo Scovazzi, The simple Shifted Fracture Method, Internat. J. Numer. Methods Engrg. 124 (2023) 2837–2875.
[37] Chuanqi Liu, WaiChing Sun, Shift boundary material point method: an image-to-simulation workflow for solids of complex geometries undergoing large deformation, Comput. Part. Mech. 7 (2) (2020) 291–308.
[38] Tianju Xue, WaiChing Sun, Sigrid Adriaenssens, Yujie Wei, Chuanqi Liu, A new finite element level set reinitialization method based on the shifted boundary method, J. Comput. Phys. 438 (2021) 110360.
[39] Alexander G. Belyaev, Pierre-Alain Fayolle, On variational and PDE-based distance function approximations, Comput. Graph. Forum (Wiley Online Libr.) 34 (8) (2015) 104–118.
[40] Frederick T. Wall, Statistical thermodynamics of rubber. II, J. Chem. Phys. 10 (7) (2004) 485–488.
[41] C.H. Liu, G. Hofstetter, H.A. Mang, 3D finite element analysis of rubber–like materials at finite strains, Eng. Comput. 11 (2) (1994) 111–128.
[42] M. Cervera, M. Chiumenti, R. Codina, Mixed stabilized finite element methods in nonlinear solid mechanics: Part I: Formulation, Comput. Methods Appl. Mech. Engrg. 199 (37) (2010) 2559–2570.
[43] M. Cervera, M. Chiumenti, R. Codina, Mixed stabilized finite element methods in nonlinear solid mechanics: Part II: Strain localization, Comput. Methods Appl. Mech. Engrg. 199 (37) (2010) 2571–2589.
[44] M. Cervera, M. Chiumenti, L. Benedetti, R. Codina, Mixed stabilized finite element methods in nonlinear solid mechanics. Part III: Compressible and incompressible plasticity, Comput. Methods Appl. Mech. Engrg. 285 (2015) 752–775.
[45] N.M. Lafontaine, R. Rossi, M. Cervera, M. Chiumenti, Explicit mixed strain-displacement finite element for dynamic geometrically non-linear solid mechanics, Comput. Mech. 55 (3) (2015) 543–559.
[46] M. Cervera, N. Lafontaine, R. Rossi, M. Chiumenti, Explicit mixed strain–displacement finite elements for compressible and quasi-incompressible elasticity and plasticity, Comput. Mech. 58 (3) (2016) 511–532.
[47] Guglielmo Scovazzi, Ting Song, Xianyi Zeng, A velocity/stress mixed stabilized nodal finite element for elastodynamics: Analysis and computations with strongly and weakly enforced boundary conditions, Comput. Methods Appl. Mech. Engrg. 325 (2017) 532–576.
[48] J.C. Simo, F. Armero, R.L. Taylor, Improved versions of assumed enhanced strain tri-linear elements for 3D finite deformation problems, Comput. Methods Appl. Mech. Engrg. 110 (3–4) (1993) 359–386.
[49] Juan-Carlos Simo, Francisco Armero, Geometrically non-linear enhanced strain mixed methods and the method of incompatible modes, Internat. J. Numer. Methods Engrg. 33 (7) (1992) 1413–1449.
[50] Robert L. Taylor, A mixed-enhanced formulation tetrahedral finite elements, Internat. J. Numer. Methods Engrg. 47 (1–3) (2000) 205–227.
[51] Eric P. Kasper, Robert L. Taylor, A mixed-enhanced strain method: Part I: Geometrically linear problems, Comput. Struct. 75 (3) (2000) 237–250.
[52] Ludovic Noels, Raul Radovitzky, A general discontinuous Galerkin method for finite hyperelasticity. formulation and numerical applications, Internat. J. Numer. Methods Engrg. 68 (1) (2006) 64–97.
[53] Alex Ten Eyck, Adrian Lew, Discontinuous Galerkin methods for non-linear elasticity, Internat. J. Numer. Methods Engrg. 67 (9) (2006) 1204–1243.
[54] Adrian Lew, Patrizio Neff, Deborah Sulsky, Michael Ortiz, Optimal BV estimates for a discontinuous Galerkin method for linear elasticity, Appl. Math. Res. Express 2004 (3) (2004) 73–106.
[55] Béatrice Riviere, Simon Shaw, Mary F Wheeler, John R Whiteman, Discontinuous Galerkin finite element methods for linear elasticity and quasistatic linear viscoelasticity, Numer. Math. 95 (2) (2003) 347–376.
[56] Béatrice Riviere, Mary F. Wheeler, Optimal error estimates for discontinuous Galerkin methods applied to linear elasticity problems, in: Comput. Math. Appl., Citeseer, 2000.
[57] F. Brezzi, M. Fortin, Mixed and Hybrid Finite Element Methods, Springer Series in Computational Mathematics, vol. 15, Springer, 1991.
[58] T.J.R. Hughes, G.R. Feijóo, L. Mazzei, J.B. Quincy, The variational multiscale method– a paradigm for computational mechanics,, Comput. Methods Appl. Mech. Engrg. 166 (1) (1998) 3–24.
[59] C. Tong, R. Tuminaro, ML2.0 Smooth Aggregation User's Guide, Technical report, Sandia National Laboratories, Albuquerque, New Mexico, 2000.
[60] J.C. Simo, M.S. Rifai, A class of mixed assumed strain methods and the method of incompatible modes, Internat. J. Numer. Methods Engrg. 29 (8) (1990) 1595–1638.
[61] Imperial College Consortium on Pore-scale Modelling, LV60A sandpack, 2014, https://figshare.com/articles/LV60A_sandpack/1153795.